Planar Multilayer Thin Film Coatings for Passive Winter Thermal Management

by

Muhammad Saad Asad

A thesis submitted to the Department of Electrical & Computer Engineering

In conformity with the requirements for

the degree of Master of Applied Science

Queen's University
Kingston, Ontario, Canada
December, 2021

Abstract

Buildings are responsible for 40% of global energy consumption. 76% of that energy is spent on comfort control including heating, cooling and ventilation. This large energy consumption results in significant greenhouse gas emission, which adversely affects the global climate. The high cost of fossil fuel also causes widespread energy poverty. Adoption of passive heating schemes which utilize solar energy for indoor heating can greatly reduce the energy requirement of buildings in the cold climate. Currently available passive heating schemes often require significant investment and they cannot be easily retrofitted to existing buildings. Windows are a major source of heat loss in a typical building in the cold climate. Development of transparent solar energy harvesting coatings for windows can play a major role in reducing energy consumption and fuel costs. In recent years, there has been a great research effort towards designing transparent solar absorber coatings using nanophotonic structures for passive heating of windows. These coatings are highly efficient and can be retrofitted to existing windows. However, the nanophotonic designs proposed so far either require expensive materials for their implementation or require expensive fabrication processes, which are difficult to scale up. The objective of this thesis is to explore designs of transparent solar absorber coatings for windows which will overcome the limitations of previously reported nanophotonic designs. We investigate the applicability of planar multilayer thin films consisting of low cost materials for this purpose. Our study led to the proposals of two designs that predict temperature rise of 21 K and 25 K, while maintaining mean visible transmittance over 60%. We experimentally observed 6.9 K rise in temperature under sunlight for our design, which compares favorably against previously reported designs which are significantly more expensive and difficult to implement. The performance of our designs is expected to improve significantly if the fabrication process is optimized. These results illustrate the great promise that nanophotonics holds for the reduction of energy consumption of buildings, which will be a significant step towards helping the environment and improving the quality of life of people in many countries around the world.

Acknowledgements

I would like to extend my sincere gratitude to my supervisor Prof. Muhammad Zulfiker Alam. His unwavering kindness, support and guidance have helped me through this journey. I am very fortunate to have had the great privilege of being mentored by someone of his caliber. He has always been approachable and his dedication to his students is something I am incredibly grateful for.

I would like to thank Dr. Graham Gibson for his help with fabrication. I also wish to thank Prof. Karin Hinzer and her research group for allowing me to use their lab resources at the University of Ottawa. I would also like to extend my gratitude to Dr. Jawad Siddiqui for his feedback about the thesis. I also want to thank my colleagues Mir Mehedi Al Hammadi and Kazi Afsara Taher for their friendship. During my time at Queen's, I appreciate all the administrative support that I received from Debra Fraser and Cheryl Wright. Finally, I would like to thank my parents, younger sister and brother for supporting me through this journey.

Table of Contents

List of Figures

List of Tables

List of Abbreviations

BWA	Bang-Bang Weighted Aggregation
CVD	Chemical Vapor Deposition
CWA	Conventional Weighted Aggregation
DWA	Dynamic Weighted Aggregation
FDTD	Finite Difference Time Domain
HEAT	Heat Transport
IMIMI	Insulator/Metal/Insulator/Metal/Insulator
IR	Infrared
Low-E	Low Emissivity
NIR	Near Infrared
MIM	Metal/Insulator/Metal
PDLC	Polymer Dispersed Liquid Crystal
PDMS	Polydimethylsiloxane
PMMA	Poly (methyl methacrylate)
PSO	Particle Swarm Optimization

Chapter 1

Introduction

The purpose of the thesis is to develop a low-cost transparent coating to utilize solar energy for heating of buildings in cold climate, which will reduce use of fossil fuel and energy poverty. In the following we will describe the motivation behind this work, the contributions of this research work and the organization of this thesis.

1.1 Motivation

Reduction of global greenhouse gas emission is essential to avoid catastrophic change of global climate. Buildings are responsible for 40% of global energy consumption and 76% of that energy is spent on comfort control including heating, cooling and ventilation [1]. Heating of building in cold climate is the most significant component of this energy consumption in the developing world [2]. In recognition of the importance of reducing the energy consumption of buildings, the Paris Agreement stipulated that the energy consumption of new buildings needs to be reduced by 80% by 2020 [3]. This goal was very aggressive and most countries failed to meet it. New technologies that can be adopted by both existing and new buildings will be a major step toward reduction of global greenhouse gas emission and also help meet regulatory requirements in the future.

Energy poverty defined as a condition, where more than 10% of household income is spent on energy. The high price of fuel is the cause of widespread energy poverty around the world. In the winter of 2012/13, more than 15,000 deaths in the UK alone were due to lack of affordable home heating [4]. Energy poverty in the UK has grown by 51% since then and now affects one in every

four households. The situation in Canada is very similar. One in every five households in Canada spent an average of 12% of their income on utilities in 2011 [5]. With rising electricity costs, the energy poverty in Canada most likely has become even worse. The situation is very similar in other countries. Currently more than 60% people in several European countries are suffering from energy poverty and struggling to pay for the heating cost this winter [6]. Developing a low-cost technology to harvest solar energy for heating of buildings will greatly improve the comfort and living condition for poor people in the cold climate.

Although solar energy has been used for centuries for heating of buildings, its potential has traditionally been vastly underestimated and it has played a relatively minor role in overall thermal management of buildings. Several studies in last few decades have changed this perception [2]. In the mid-1980's, field investigations across Europe showed that the solar energy captured for indoor heating of buildings in coastal northern climates was much higher than that captured in sunnier southern climates. This finding was later explained by the fact that the longer, cloudier heating seasons extended into spring and fall months with numerous hours of daylight. A very recent study has calculated the magnitude and distribution of solar energy overlapping with space-heating needs in the US by taking into account data for solar radiation, outdoor temperature and heating energy use. Solar energy available for heating of residential areas in several metropolitan cities including Detroit and Boston (cold continental), Washington D.C. (humid subtropical), Seattle and San Francisco (Mediterranean), and Denver (semi-arid) was found to be 5 TWh [2]. Projection of these results indicates that 750 TWh solar energy is available for meeting the heating needs of buildings in the US. Proper utilization of currently available passive heating technology will meet one third of total residential heating requirement in the US (1200 TWh). Development of new passive heating technology and its widespread adoption to utilize the untapped potential of this huge resource will have a huge impact on global energy crisis, energy poverty and create huge economic opportunities.

Current methods of passive heating including double glazed window, Trombe wall and solarium have several limitations. They often require significant investment and cannot be easily retrofitted to existing buildings. Recent progress of nanophotonics has created new opportunities for passive heating that can overcome some of the limitations of existing alternatives. These designs are highly efficient, can provide great flexibility in controlling the transmission and absorption spectrum of light over a broad wavelength range, can be retrofitted over existing buildings, and can be potentially less expensive. However, the technology in still in its nascent state and more work is necessary to make a make it viable for real life applications.

1.2 Objectives and Contributions

The objective of this thesis is to develop a low-cost window coating for passive heating of buildings that can be fabricated with simple fabrication process. Our work led to the following accomplishments:

1) Design of planar multilayer coating for passive heating: We proposed designs based on planar multilayer architecture using low cost plasmonic materials. These designs can be fabricated using simple and scalable fabrication process. They outperform many previous designs which are more expensive and difficult to fabricate in terms of heating potential.
2) Experimental demonstration of passive solar heating: We experimentally demonstrated significant temperature rise for our design under solar illumination.

1.3 Organization

Chapter 2 presents a brief overview of the current state of the art technology for passive heating of buildings. We review both established and emerging methods to achieve this goal. Advantages and limitations of these methods and the need for developing a new nanophotonic passive heating scheme are described.

Chapter 3 is on modeling methods used in this thesis. In this work we used transfer matrix method for analyzing the optical properties of the multilayer structures we designed, and used particle swarm optimization (PSO) to optimize our designs. The thermal characteristics of the optimized device was investigated using Heat Transport (HEAT) solver from Lumerical. Principle of operation of these methods are presented in this chapter.

Chapter 4 presents details of our proposed transparent solar absorber designs. We carried out a detailed investigation using transfer matrix formulation and PSO to determine the optimum choice of materials and dimensions. We carried out thermal simulations to estimate the temperature rise achievable for the optimized designs under solar illumination.

Chapter 5 presents the details of fabrication and measurement results for the designs described in Chapter 4. Results for both optical and thermal characterizations are presented.

Chapter 6 concludes the thesis with a few closing remarks and suggestions for possible future extensions of this work.

Chapter 2

Literature Review

The focus of this thesis is the development of a window coating technology for passive heating. The increasing recognition of the importance of passive heating for reducing environmental impact of buildings and energy poverty has led to many innovations in this research area in recent years. This chapter presents an overview of various passive heating methods employed for buildings. We start by reviewing the concept of sustainable heating and explain the role of passive heating in this context. We then review some of the well-established strategies for passive heating. This is followed by a review of recent progress on nanophotonics based passive heating. The review we present is brief as its purpose is to provide context for the work presented in this thesis.

2.1 Sustainable Heating

The goal of sustainable heating technology is to reduce dependence on fossil fuels for indoor heating and help in the effort to make building self-sustainable in terms of generating their own energy for heating. Sustainable heating can be classified into three broad categories: maximization of heat retention, passive solar heating and mechanical heating as illustrated in Fig. 2.1 [7].

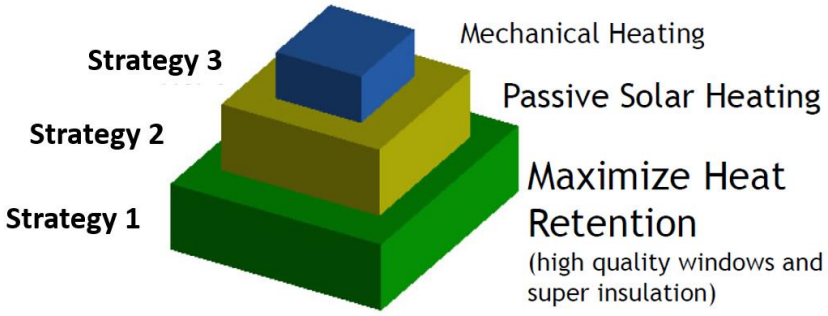

Fig. 2.1: Sustainable heating strategies [7].

The first strategy of sustainable heating involves minimizing heat escape from an indoor space. This is often done by installing layers of insulating materials on walls of the building. Minimizing heat escape through the window is more challenging since the requirement of maintaining high transmission imposes significant design restrictions. For typical residential and commercial buildings, windows are often responsible for more than 25% of heat loss [8].

The second strategy known as passive solar heating aims at utilization of solar energy for heating of buildings. There are two different approaches for passive heating. The first approach utilizes absorption of solar energy over the entire solar spectrum to achieve heating and is suitable for heating of opaque structures including the walls of buildings. The second approach engineers the transmission and absorption over the entire solar spectrum to simultaneously achieve large transmission in the visible and large overall absorption, and is suitable for heating of windows. As illustrated in Fig. 2.2, more than 50% of the solar power lies within the ultraviolet (UV) and near-infrared (NIR) regions which does not contribute to illumination [9]. Efficiently harvesting these portions of the solar spectrum for indoor heating purpose can allow considerable energy savings.

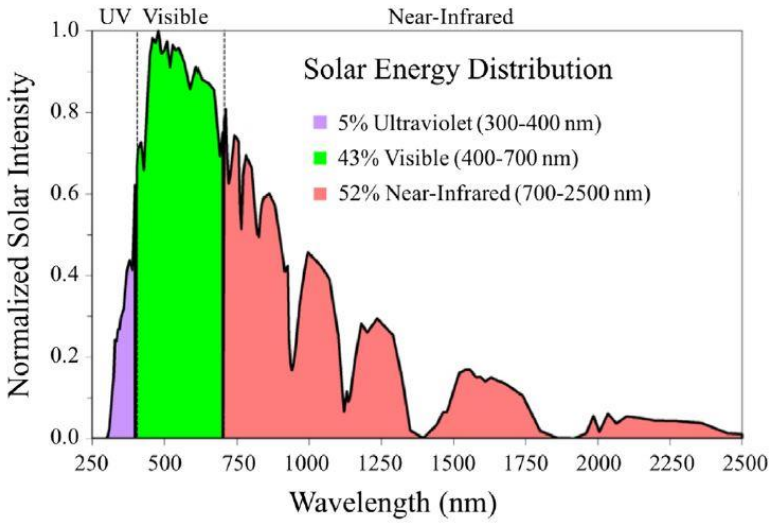

Fig. 2.2: Energy distribution of the solar spectrum [9].

The third strategy known as mechanical heating involves designing mechanical and electrical heating equipment such as furnaces, boilers, heat pumps and air ducts to be as efficient as possible to reduce energy consumption of buildings. Strategy 3 is beyond the scope of this thesis and will not be discussed further. Interested reader can find more information regarding this strategy from [10].

2.2 Conventional Passive Heating Strategies

Passive heating has been used since ancient times for buildings in cold climate. Many different approaches regarding design of building architecture for this purpose have been explored. These approaches can be classified as either direct or indirect gain [10].

2.2.1 Direct Gain

In this approach, sunlight is allowed to enter the interior of a house through openings or windows, which subsequently heats up the walls, floors and air (Fig. 2.3). Direct gain is the simplest and most

commonly used method of passive heating in cold climate. One widely used method to achieve heating through direct gain is by using double-glazed windows. Such a window consists of two glass panes separated by an air gap. Sunlight is directly transmitted through the glazing whereas the air gap prevents heat loss through conduction as air is a poor conductor of heat. Such windows can reduce heat loss by upto 28%.

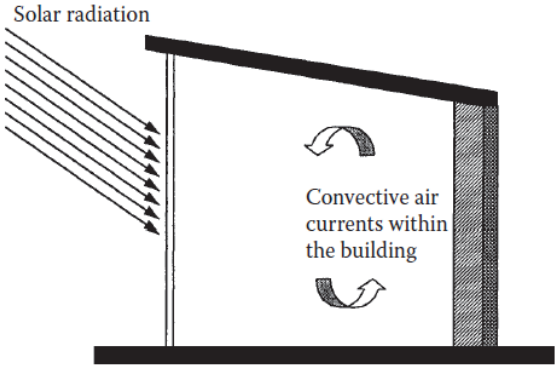

Fig. 2.3: Concept of direct passive heating [10].

2.2.2 Indirect Gain

This approach involves first collecting thermal energy from the sunlight entering a building by using thermal massed structures, and then subsequently releasing this thermal energy to an indoor space. Solar energy absorbed by the thermal mass is used to heat an indoor space using the processes of convection and conduction. Most common examples of indirect gain are the thermal storage wall, solarium and the thermal storage roof (Fig. 2.4).

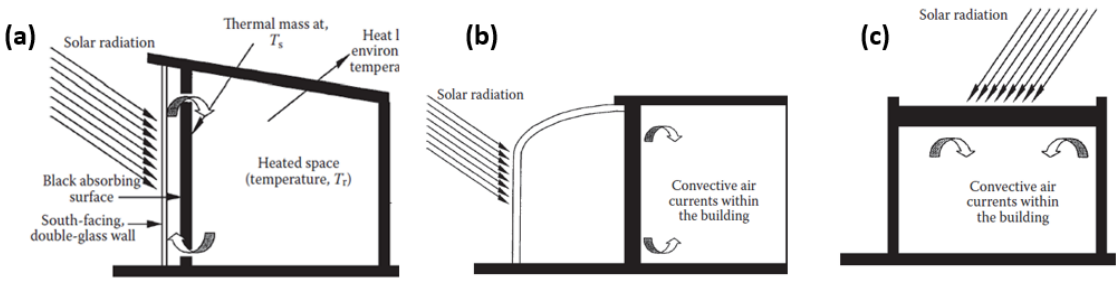

Fig. 2.4: Concepts of indirect passive heating (a) thermal storage wall (b) solarium (c) thermal storage roof [10].

In the case of thermal storage wall, light transmits through a glazed window and is absorbed by a wall placed between the glazing and the place to be heated. The absorbing wall is often a blackened masonry (Trombe wall) or water filled containers (water wall). Passive heating using solarium unifies the concepts of direct and indirect gain. Solarium can be divided into three sections which are the sunspace, the linking space and the living space. Using the method of direct heat gain, the sunspace absorbs and collects solar energy entering a window glazing. The absorbed solar energy is used to warm the indoor air. The linking space consists of a thermal wall that absorbs solar energy through the process of indirect heat gain. The thermal wall helps with heat retention and heat distribution to the indoor living space. The thermal roof, also known as the roof pond is similar to thermal storage wall, but instead of a wall, the thermal storage mass is placed on top of the roof.

2.3 Nanophotonics for Passive Heating

Although the approaches presented in the previous section have been well-known for a long time, they have certain limitations. Implementation of many of these technologies require significant investment. It is also difficult to retrofit existing buildings with these schemes. Such limitations have hindered their widespread adoption, especially in low-income settings.

In recent years, the field of nanophotonics has offered new ways of achieving improved control over light matter interaction, which created many exciting opportunities for passive heating. Such technology allows the possibility of designing window coatings that are able to control and harvest solar energy for passive indoor heating applications and overcome limitations of current passive heating technologies. Passive heating using nanophotonics falls under Strategy 1 and Strategy 2 for sustainable heating. The major types of nanophotonics based passive heating schemes will be briefly reviewed in the following sections.

2.3.1 Low Emissivity (Low-E) Coatings

Emissivity is defined as the ratio of energy radiated from a material's surface to that radiated from a perfect emitter i.e. from a blackbody at the same temperature, wavelength and the same viewing condition. According to Kirchhoff's law of the thermal radiation, at thermal equilibrium, the amount of heat emitted and absorbed by an object are equal to each other. Low-E coatings are specially designed coatings that reflect strongly in the infrared (IR) wavelengths (low absorption and consequently low emissivity of heat, and hence the name Low-E coating), while maintaining high transmission in the visible region. In hot weather, such a window can block heat from entering a building. In contrast, in cold weather, it prevents heat leakage from the interior of a building. Therefore, it helps keep a house cool in the summer and warm in the winter.

Low-E coating has been a very active area of research for last few decades and a large number of structures have been reported [11-23]. Commercial low-E coatings can be classified into two categories: hard and soft coatings. Hard coatings are metal oxide coatings applied to glass at high temperature when glass is molten and the coating becomes an integral part of the glass. Soft coatings are composed of alternate metal-dielectric layers, which are deposited using low temperature (below 200°C) processes such as CVD and sputtering. Soft coatings outperform hard

coatings in several ways such as having lower emissivity, non-hazy appearance and require much less materials for fabrication. The earliest low-E coatings were composed of one layer of Ag and two dielectric (ceramic) layers in a five-component stack. The Ag film reflects infrared and ultraviolet light, while the dielectric layers act as antireflection coatings enabling visible light to pass through. A major progress in low-E coating technology was the introduction of the double-Ag-coated glass in the early 1990s. These coatings maintain the same levels of visible light transmittance as single layer Ag low-E coatings while increasing the reflectivity of infrared light by more than 30%. Triple layer low-E coatings were introduced in 2005. These coatings can transmit 70% of the solar spectrum and can block up to 75% of infrared light. The most advanced low-E coatings use 4 layers of Ag film. They can transmit more than 50% of visible light, and reflect more than 80% infrared light [15].

Ag is a relatively expensive metal and oxidizes easily, which may limit lifetime of passive heating schemes that utilize Ag. An alternative design using low cost materials such as Cu and TiO_2 was reported in [19]. The design achieved 90% visible transparency and 85% NIR reflectance. However, mid IR reflectance, which is more important to avoid heat loss of buildings was not reported for this design.

2.3.2 Transparent Solar Absorber

While low-E coatings focus on minimizing heat loss from buildings, they do not utilize solar energy for additional heating. Absorption of solar energy for various applications has also been a very active area of research. Many recent works in this area have focused on achieving complete absorption on an opaque surface for various purposes including water desalination [24] and solar thermo-photovoltaics [25]. With increasing recognition of the need for improving energy efficiency

of buildings, there have been many reports on design and demonstration of transparent solar absorber coatings. These works fall under two broad categories: those based on nanoparticles and those based on periodic arrangements of nanostructures.

Nanoparticles exhibit unique features compared to their bulk counterparts and offer many exciting opportunities in numerous applications including drug delivery, catalysis, solar cells, biosensing, and passive heating. Unlike thin film based structures, they can often be fabricated using simple solution based processes, which enhance their commercial viability. One of the well-known designs [26] applied antimony-doped tin oxide nanoparticles to achieve large transmission in the visible and high NIR absorption. The surface resistivity of the developed transparent heat insulation coatings was 11 orders of magnitude, which allowed high radio wave transmission. There have been many reports on transparent coatings based on nanoparticles and nanocomposites, for example, coatings based on indium-doped tin oxide (ITO) nanoparticles [27], $CsWO_3$ nanoparticles [28, 29], flexible transparent coating technology based CuS-PDMS nanocomposite films [30] and polymer dispersed liquid crystal (PDLC) coatings fabricated on Ag nanowire electrode network [31]. A very recent work [32] has demonstrated the use of worm-like Au nanostructures for selective solar absorption. This design uses much less materials compared to other nanoparticle based designs. The authors experimentally demonstrated visible transparency over 65% and 9.8K increase in temperature under solar illumination.

Metasurface is a relatively new optical design methodology which uses periodic arrangements of small optical elements to achieve improved control on the properties of light. Metasurfaces can be useful for implementation of a wide range of new optical devices, for example, flat lenses, optical phased array, and new holographic schemes capable of providing high resolution and wide field of view [33]. The improved control on the properties of light can also be very useful for the realization

of transparent solar absorbers. Some of the recent designs of transparent solar absorbers using metasurface are shown in Fig. 2.5. [34] reported a metasurface consisting of periodic arrangement of nanoantennas to achieve large transmission and uniform transmission in the visible, while absorbing most of the NIR light. They considered several antenna designs consisting of multilayer stack of SiO_2 and Au as well as Al_2O_3 and Ni. Their best design was elliptical antennas based on Ni. With this design they experimentally demonstrated 8K rise in temperature under one sun.

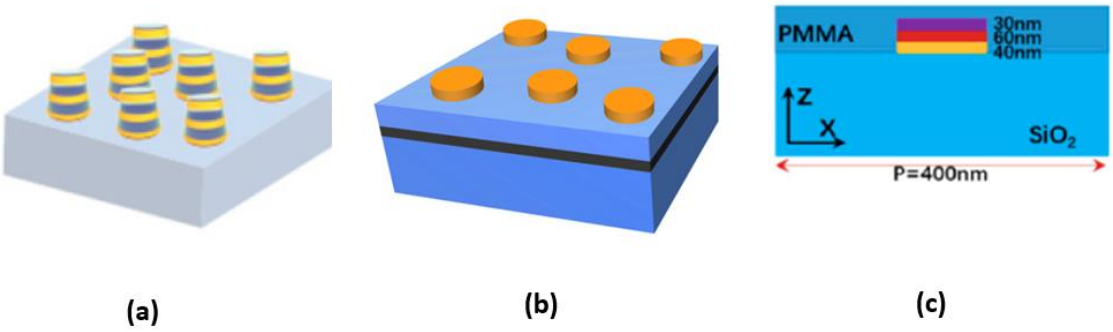

Fig. 2.5: Various metasurfaces for passive heating (a) Ni nanoantenna array [34] (b) Cu nanoantenna array [35] (c) Asymmetric metasurface [36].

Operation of most solar absorbers including that reported in [34] are not very sensitive to the direction of solar illumination, and exhibit the same transmission and comparable absorption response irrespective of whether sunlight is incident on the coating from the forward or backward direction. Although such a coating will be useful for heating in the winter, its presence will also result in undesirable heating in the summer. Several recent works have attempted designs that satisfy the following properties: (i) high visible transparency, (ii) high NIR absorption for front illumination and (iii) high NIR reflection for backside illumination. A window that has a coating with these properties is highly effective for passive heating when the coating faces the sun, but that effect can be minimized by simply reversing the orientation of window. A metasurface for

directional thermal management of windows was reported in [35]. The structure consists of periodic arrangements of Cu nanodisks separated from a thin Ag film by a glass spacer. With this design, the authors demonstrated 25% difference in absorption for illumination from different sides. Another metasurface for directional passive heating was proposed in [36]. The structure consists of periodic arrays of $Ti/Al_2O_3/Ag$ on an SiO_2 substrate and covered with a PMMA coating. Simulation results predicted 20% difference in absorption for front and back illumination for the design. Thermal performance and directivity of the design was retained when Au was replaced with Cu. The designs proposed in [35, 36] are proof of principle demonstrations of the feasibility of directional passive heating, but more work is necessary to make them acceptable for practical applications.

Transparent passive heating coatings based on metasurface designs have also been utilized for antifogging and de-icing applications [37-39]. The authors of [37] demonstrated a hybrid plasmonic metasurface based on Au nanoparticles in TiO_2 matrix to achieve temperature increase by more than 10K in order to inhibit the formation of ice at the air-solid interface. [39] investigated a photothermal coating based on Cs-doped WO_3 and benzotriazole nanoparticles embedded in a resin film for antifogging applications. The coating provided visible transmittance of above 82%, broadband UV to NIR absorption greater than 90% and raised steady state surface temperature by 38K. The coating was fabricated using simple fabrication process and showed excellent stability. Unfortunately, Cs is a rare earth material, and due to its scarcity and usefulness, it has been classified as a critical mineral for US national security and economy. It seems unlikely that Cs based designs will be widely used for passive heating applications at large scale.

Transparent photovoltaics is another very promising path for solar energy harvesting. These cells are usually fabricated using organic materials that allow visible light to transmit and produce

electricity by absorption of UV and NIR light [40,41]. Efficiency and long-term stability needs to be improved further for this technology becomes feasible for most real-life applications.

Table 2.1: Summary of major works on transparent solar absorbers.

Reference	Coating design	Optical transmittance	Optical absorption	Temperature rise (K)
[34]	Plasmonic nanoantennas based on Ni	75% (A, M)	-	8 (1 sun)
[35]	Cu plasmonic nanodisk array	40% (A, P)	75% (P, M)	-
[36]	Periodic MIM units based on Cu and Ti	60% (A, S)	45% (A, S)	
[32]	Linear assemblies of Au and Ag nanoparticles	65% (A, M)		9.8 (natural solar illumination)
[37]	Au nanoparticles embedded in TiO_2	37% (A, M)	36% (A, M)	6
[38]	Au nanoparticles embedded in TiO_2	-	36% (A, M)	3.8 (1 sun) 15.4 (4 suns)
[39]	Cs-doped nanoparticles embedded in resin	82% (P, M)	Above 90% (P, M)	38

* M: Results from measurement, S: Results from simulation, A: Average, P: Peak

Several conditions must be simultaneously satisfied before widespread adoption of transparent solar absorbers for heating of buildings becomes economically feasible and acceptable by the community. The design must provide a good compromise between visible transmission and overall absorption. It must use only inexpensive and readily available materials. It needs to be easy to fabricate with simple, low cost scalable process. The materials used to implement the structure will ultimately end up either in landfills or end up in lakes and rivers. To minimize the environmental impact, the design should minimize the amount of potentially harmful nanomaterials needed for its implementation. Unfortunately, none of the designs proposed to date can satisfy all these

requirements. The designs based on metasurfaces show excellent performance, but the requirement of periodicity necessitates the use of expensive and nonscalable fabrication processes. In addition, these designs often require noble metals (Au or Ag) which makes them prohibitively expensive for large scale applications. Designs based on nanoparticles can be fabricated using simpler processes. These structures are however significantly thicker and require more material compared to designs based on metasurface. For example, the Ni thickness in the metasurface proposed in [34] is 20 nm, whereas the thickness of the active layer for the nanoparticle based design reported in [26] are several microns. The large thickness of these designs makes them costly and environmentally more harmful if used at large scale.

Nanophotonic approach has also been used to achieve daytime cooling of buildings [42, 43]. Although these works offer great promises for reduction of fuel cost and greenhouse gas emission, they fall outside the scope of this thesis, and will not be reviewed further.

Chapter 3

Design Methodology

The aim of this thesis is to develop a window coating which will allow high transmission of visible light while also have the ability of achieving significant temperature rise under solar illumination. The design of such a coating requires a combination of suitable optical and thermal simulation methods, and an optimization scheme. The optical simulation for this work was carried out mostly using transfer matrix method. We used particle swarm optimization (PSO) method for optimizing the design and used Lumerical HEAT for the thermal simulation. This chapter introduces the key concepts of these techniques.

3.1 Transfer Matrix Method

The research work for this thesis focuses on planar multilayer structures consisting of metals and dielectrics. Transfer matrix method is a semi-analytical method that can provide accurate results for the optical properties of such structures. It is very fast and works well for any choice of polarization, arbitrary layer thicknesses and material properties. Therefore, we chose to use transfer matrix for our analysis. We briefly explain the principle of transfer matrix method with the example of propagation of an electromagnetic wave through the multilayer stack shown in Fig. 3.1. The description presented here closely follows that of [44, 45]. The structure shown in Fig. 3.1 consists of N layers of finite thickness, where the thickness and refractive index of layer i $(i = 1,2, \dots, N)$ is d_i and $\hat{n}_i$ respectively. In general, complex refractive index $\hat{n}_i$ is represented by $\hat{n}_i = n_i + jk_i$ where n_i is the real part of the refractive index and k_i is the extinction coefficient. The multilayer stack is sandwiched between two semi-infinite media having refractive indices $\hat{n}_0$ and $\hat{n}_{N+1}$. θ_i

denotes the angle at which light is refracted into media i from media $i-1$ as it propagates from left to right.

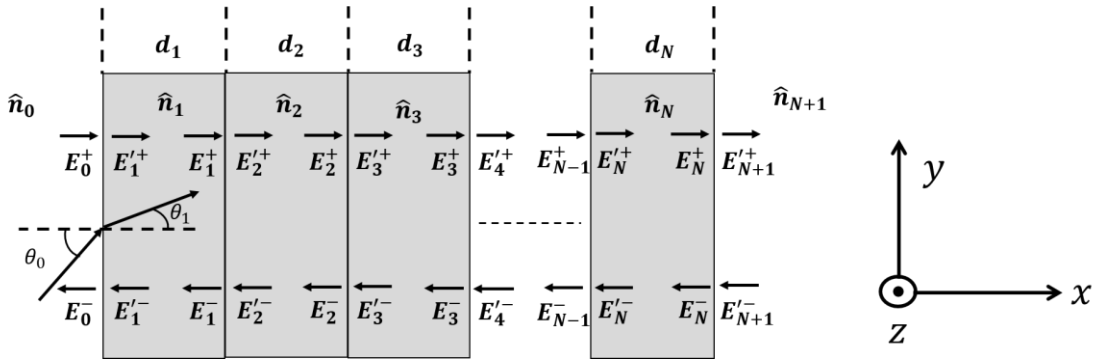

Fig. 3.1: Multilayer stack consisting of $\boldsymbol{N}$ layers of finite thicknesses.

By applying boundary conditions for electric and magnetic fields, it can be shown that the electric fields at the two sides of the boundary between layer i and $i+1$ are related as shown below

$$\begin{pmatrix} E_i^+ \\ E_i^- \end{pmatrix} = D_{i,i+1} \begin{pmatrix} E_{i+1}'^+ \\ E_{i+1}'^- \end{pmatrix} \tag{3.1}$$

The matrix $D_{i,i+1}(i = 0,1,\dots,N)$ can be expressed in terms of the Fresnel reflection $r_{i,i+1}$and transmission $t_{i,i+1}$ coefficients

$$D_{i,i+1} = \frac{1}{t_{i,i+1}} \begin{bmatrix} 1 & r_{i,i+1} \\ r_{i,i+1} & 1 \end{bmatrix} \tag{3.2}$$

For a TE or s-polarized incident wave (electric field confined in the yz plane), these quantities are given by

$$r_{i,i+1} = \frac{\hat{n}_i cos\theta_i - \hat{n}_{i+1} cos\theta_{i+1}}{\hat{n}_i cos\theta_i + \hat{n}_{i+1} cos\theta_{i+1}} \tag{3.3}$$

$$t_{i,i+1} = \frac{2\hat{n}_i cos\theta_i}{\hat{n}_i cos\theta_i + \hat{n}_{i+1} cos\theta_{i+1}} \tag{3.4}$$

For a TM or p-polarized incident wave (magnetic field confined in the yz plane), these coefficients are given by

$$r_{i,i+1} = \frac{\hat{n}_i cos\theta_{i+1} - \hat{n}_{i+1} cos\theta_i}{\hat{n}_i cos\theta_{i+1} + \hat{n}_{i+1} cos\theta_i} \tag{3.5}$$

$$t_{i,i+1} = \frac{2\hat{n}_i cos\theta_i}{\hat{n}_i cos\theta_{i+1} + \hat{n}_{i+1} cos\theta_i} \tag{3.6}$$

The electric fields at the left and right side of the ith layer are related by the propagation matrix P_i $(i = 1,2, \dots, N)$

$$\begin{aligned} \begin{pmatrix} E_i'^{+} \\ E_i'^{-} \end{pmatrix} &= P_i \begin{pmatrix} E_i^{+} \\ E_i^{-} \end{pmatrix} \\ &= \begin{bmatrix} e^{-j\varphi_i} & 0 \\ 0 & e^{+j\varphi_i} \end{bmatrix} \begin{pmatrix} E_i^{+} \\ E_i^{-} \end{pmatrix} \end{aligned} \tag{3.7}$$

Where φ_i is the phase shift experienced by the wave when it propagates a distance d_i through the ith layer, and has the following expression

$$\varphi_i = \frac{2\pi}{\lambda} \hat{n}_i d_i cos\theta_i \tag{3.8}$$

The electric field entering and exiting the multilayer stack shown in Fig. 3.1, are related as follows

$$\begin{pmatrix} E_0^{+} \\ E_0^{-} \end{pmatrix} = M \begin{pmatrix} E_{N+1}'^{+} \\ E_{N+1}'^{-} \end{pmatrix} \tag{3.9}$$

Where the matrix M represents the bulk action of all layers present in the multilayer stack and is given by

$$M = \begin{pmatrix} M_{11} & M_{12} \\ M_{21} & M_{22} \end{pmatrix} = D_{0,1} P_1 D_{1,2} P_2 D_{2,3} P_3 \dots P_N D_{N,N+1} \tag{3.10}$$

The transfer matrix M can be used to determine the overall reflectance R and transmittance T of the multilayer stack using the following expressions

$$R = \left|\frac{M_{21}}{M_{11}}\right|^2 \tag{3.11}$$

$$T = \frac{n_{N+1}cos\theta_{N+1}}{n_0 cos\theta_0}\left|\frac{1}{M_{11}}\right|^2 \tag{3.12}$$

The absorption of the structure can be found using the relation

$$A = 1 - R - T \tag{3.13}$$

3.2 Particle Swarm Optimization

The interaction of light with even relatively simple multilayer structure can be quite complex [45]. As the number of layers and design variables increase, the complexity of the design space increases rapidly. Hence there is a need to utilize an optimization algorithm to efficiently scan through possible solutions and find the optimal one.

Optimization techniques inspired by swarm intelligence have become increasingly popular during the last decade. These algorithms take inspiration from the social behavior of insects and animals such ant colonies, flock of birds, animal herding, bacterial growth and school of fishes. They are more robust and flexible compared to many traditional optimization techniques. The two most popular optimization algorithms that utilize swarm intelligence are ant colony optimization and particle swarm optimization. These algorithms have taken inspiration from the foraging behavior of ants [46] and behavior of flock of birds respectively [47]. Other optimization algorithms based on swarm intelligence include bacterial foraging optimization which takes inspiration from the

foraging behavior of bacteria such as E. Coli and M. Xanthus [48], artificial bee colony algorithm based on behavior of honeybees [49] and glowworm swarm optimization [50] based on the luminescence quantity of light intensity glowworms emit.

Compared to other stochastic algorithms, PSO offers a number of advantages including robustness, efficiency and simplicity. It also requires less computational effort compared to other stochastic algorithms. Since its introduction in in 1995 by Kennedy and Eberhart [47], PSO has become one of the most popular and highly investigated optimization algorithm that utilizes swarm intelligence. It has found widespread applications in many different fields ranging from language studies to engineering and applied sciences. The total number of publications related to PSO from 2010 to 2014 are greater than the sum of all publications related to six other well-known optimization algorithms based on swarm intelligence [51]. It is for these reasons we chose to utilize PSO for optimization of our designs. In the following we explain the principle behind PSO when a single objective function needs to be optimized. This is followed by the description of PSO for the case of multiple-objective functions.

3.2.1 Single-Objective Particle Swarm Optimization

The PSO algorithm works by finding the optimal regions in a complex search space through movement of individual vectors known as particles which mimic the movement of a flock of birds in air. The following description of the method for development of PSO algorithm follows that reported in [52]. To begin, we start by considering a total of ps particles with initial positions $x_{i,0}$ $(i = 1,2, \dots, ps)$ which are generated using a uniform distribution and initial velocities $v_{i,0}$ $(i = 1,2, \dots, ps)$. The position of each particle represents a potential solution to the problem and the velocity of the particle defines it's movement direction and speed through the search space.

Before the optimization begins, the initial position of the particles are stored as $pbest_{i,g}$ where g is the generation counter which is set to 0 initially. After each generation, particles update their local position $x_{i,g+1}^d$ and velocity $v_{i,g+1}^d$ according to the following relations

$$v_{i,g+1}^d = \omega_g v_{i,g}^d + c_1 rand1_{i,g}^d(0,1) \cdot \left(pbest_{i,g}^d - x_{i,g}^d\right) + c_2 rand2_{i,g}^d(0,1) \cdot \left(gbest_g^d - x_{i,g}^d\right) \tag{3.14}$$

$$x_{i,g+1}^d = x_{i,g}^d + v_{i,g+1}^d \tag{3.15}$$

The quantity $d = 1,2,\dots,D$ where D is the dimensionality which represents the number of parameters considered for optimization. The quantities $pbest_{i,g}^d$ and $gbest_g^d$ represent the local best and global best position visited so far by the movement of particles through the search space. c_1 and c_2 are the acceleration coefficients set by the user and ω_g is the inertia weight. For each ith particle and d^{th} dimension, $rand1_{i,g}^d(0,1)$ and $rand2_{i,g}^d(0,1)$ are two random numbers generated between 0 and 1. After each generation, the following three vectors are updated for the ith particle: position ($x_{i,g}^d$), velocity ($v_{i,g}^d$) and local best position ($pbest_{i,g}^d$). The optimization runs iteratively updating the position and velocity vectors for all particles as well as the global best solution ($gbest_g^d$) until the maximum number of generations set by the user is reached.

3.2.2 Multi-Objective Particle Swarm Optimization

In many practical situations, we need to simultaneously optimize multiple objective functions. For example, a window optimized for passive heating should maximize transmission in the visible region and absorption in the NIR region. PSO is particularly suitable for multi-objective optimization due to its high convergence speed for single objective optimization cases [53]. Among

the most common methods for multi-objective optimization, the global criterion method is often used. In this scheme all the objective functions are aggregated to form a single objective function. We start by considering a multi-objective optimization problem with k total objective functions $(f_i, i = 1,2, \dots, k)$. When using the weighted aggregation approach, we optimize a single scalar objective function F such that

$$F = (w_1 f_1, w_2 f_2, \dots, w_k f_k) \tag{3.16}$$

Where w_i are nonnegative weights such that

$$\sum_{i=1}^{k} w_i = 1 \tag{3.17}$$

Well known weighted global aggregation approaches include conventional weighted aggregation approach (CWA), dynamic weighted aggregation approach (DWA) and bang-bang weighted aggregation (BWA). In the CWA approach, the k objective functions are summed to form a single objective function as shown below

$$F = \sum_{i=1}^{k} w_i f_i \tag{3.18}$$

The optimization scheme is repeated with different weight configurations until a good compromise is obtained between different objective functions. In case of the DWA approach, the values of weights are gradually changed during the optimization. DWA is applied for the case when two objective functions are required to be optimized simultaneously. During optimization, the value of weights associated with each objective function change over time according to the following equations

$$w_1 = \left|\sin\left(2\pi t_g / f_c\right)\right| \tag{3.19}$$

$$w_2 = 1 - w_1 \tag{3.20}$$

Where t_g is the generation number and f_c is the frequency of weight change. The weights w_1 and w_2 change periodically from 0 to 1 during the optimization. The value of frequency f_c should be set so that the weights change from 0 to 1 at least twice during the optimization. The BWA approach is similar to DWA with the exception that weights representing the two objective functions change periodically as follows

$$w_1 = sign(\sin(\frac{2\pi t_g}{f_c})) \tag{3.21}$$

$$w_2 = 1 - w_1 \tag{3.22}$$

Although the DWA and BWA methods are known to efficiently find the optimal solution due to the fact that the weights are automatically adjusted during the optimization, the CWA approach allows the user to easily control the desired comprise between the different objective functions by manually selecting the weight configurations. Therefore, we chose to use CWA method for the optimization of our design.

3.3 Heat Transfer Modelling

To determine the rise in temperature of a window under solar illumination, all three fundamental mechanisms of heat transfer (conduction, convection and radiation) need to be taken into account. Here we briefly describe these processes.

The temperature variation through thermal conduction with respect to time can be modelled using the heat transport equation

$$\rho \cdot C_p \cdot \frac{\partial T}{\partial t} = \nabla \cdot (k \cdot \nabla T) + Q \quad (3.23)$$

Where ρ is the density of the material ($kg \cdot m^{-3}$), C_p is the specific heat capacity ($J \cdot Kg^{-1} \cdot K^{-1}$), k is the thermal conductivity ($W \cdot m^{-1} \cdot K^{-1}$), T is the temperature of the object (K), t is time (seconds) and Q is the heat source or absorbed energy (W).

At thermal equilibrium, the net absorbed power is equal to the net dissipated heat and the surface temperature of the system remains constant over time. The heat transport equation under this condition can be simplified to

$$Q = -\nabla \cdot (k \cdot \nabla T) \quad (3.24)$$

Since the window surface is in contact with air, heat loss from the window surface through process of convection will occur due to the difference in temperature between the window surface and air.

Heat loss through process of convection can be modelled using

$$Q = Ah_c(T - T_0) \quad (3.25)$$

Where A is the surface area of the object (m^2), h_c is the convective heat transfer coefficient ($W \cdot m^{-2} \cdot K^{-1}$), T_0 is the temperature of ambient air (K) and Q in this case can be thought of the heat lost due to convection.

Heat transfer through radiation is related to the temperature of the object (T) and air (T_0) and can be modelled as follows

$$\varepsilon\sigma(T^4 - T_0^4) = Q/A \quad (3.26)$$

Where ε is the emissivity of the object (dimensionless), and σ is the Stefan-Boltzmann constant ($W \cdot m^{-2} \cdot K^{-4}$). After applying the substitution $T = \Delta T + T_0$, where ΔT is the temperature difference between the object and air, equation 3.26 becomes

$$\varepsilon\sigma(\Delta T^4 + 4\Delta T^3 T_0 + 6\Delta T^2 T_0^2 + 4\Delta T T_0^3) = Q/A \tag{3.27}$$

For relatively small temperature difference ($\Delta T < 10\text{K}$ and $T_0 \approx 295\text{K}$), the terms involving high order of ΔT can be neglected, which considerably simplify equation 3.27.

$$4\varepsilon\sigma\Delta T T_0^3 = Q/A \tag{3.28}$$

Therefore, for small increase in surface temperature of the window surface after exposure to sunlight, the temperature increase will vary linearly with the absorbed solar power (W).

To accurately model the thermal performance, all these thermal processes need to be modeled accurately. In our work we used a commercial heat transport solver (Lumerical HEAT) to examine the thermal performance of the window coating. Using finite element modeling, HEAT provides extensive capability of modeling conduction, convection and radiation processes [54]. As a part of Lumerical Device Multiphysics Suite, HEAT can be easily integrated with other Lumerical packages including Lumerical FDTD. This feature will be very useful for analysis of our design detailed in the following chapter.

Chapter 4

Design and Optimization

In previous chapters, we have explained the limitations of current passive heating technology, and the need for development of nanophotonics based passive heating schemes, especially transparent coatings. We now present the details of designs of such a coating. Unlike previous works, which focused on designs involving either nanopatterns or nanoparticles, we chose to use planar multilayer structures since these structures can be fabricated using inexpensive and widely available thin film deposition techniques. This geometry has been explored for design of broadband, opaque solar absorbers [55-59] and wavelength selective filters [60], but yet to be investigated for design of transparent solar absorbers. In the following we present the design and optimization that we carried out for such coatings. Optical and thermal performance of the optimized designs are also presented.

4.1 Optimization of the MIM Solar Absorber

The optimization of our design is carried out in two steps. We start our design by focusing on the simple metal-insulator-metal geometry shown in Fig. 4.1. It consists of two thin metal layers separated by a dielectric spacer and covered with a SiO_2 protective coating. This simple geometry allows us to investigate in detail the effects of various parameters such as choice of metal and spacer medium and the effect their thicknesses have on the performance of the design. Once this structure is optimized, we used it as a starting point for a more complicated design to further improve the optical and thermal performance.

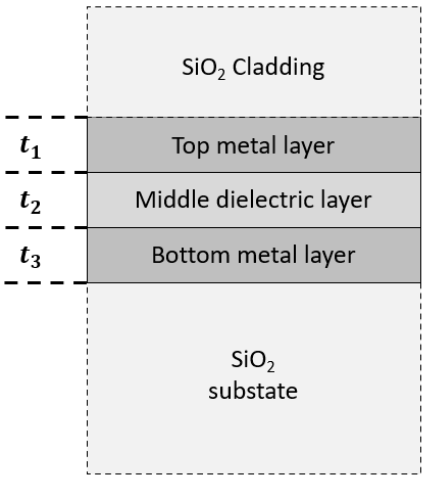

Fig. 4.1: Planar MIM design for passive heating.

To determine the optimal material choice and layer thickness of the MIM design, we first investigated different plasmonic materials for the top and bottom layers. The metal and plasmonic materials investigated are the following: Ni, Cu, Al, TiN and Au. Al is a low cost plasmonic material that has been heavily researched due to its strong plasmonic response in the visible regime [61, 62]. Ni, and Cu are low cost metals that have been studied by research groups for transparent passive heating applications [34-36]. Other than traditional metals, the transition metal nitride TiN is considered a good candidate due to its higher mechanical and thermal stability when compared to noble metals [63, 64]. Noble metals such as Au has been heavily researched for wavelength selective solar heating applications due to its strong resonance in the visible and NIR wavelength ranges. Although Au is not a practical choice for large scale applications due to its high cost, we include Au in our investigation to estimate the compromise in performance we may have to accept when using less expensive metals.

As stated earlier, since our designs are based on planar multilayer MIM stacks, transfer matrix formulation together with PSO was used for the optimization. The transfer matrix method was

implemented using MATLAB. The accuracy of this code was verified by comparing the results obtained from this code with those obtained from Lumerical STACK from Ansys. Optical properties of Cu, Al and Au were taken from [65], and those for Ni were taken [66]. For TiN, the refractive index data was obtained from [67, 68]. The dielectric spacer region separating the metallic layers for this analysis is assumed to be SiO_2. Optical properties of SiO_2 were taken from [66]. Effect of the choosing other spacer materials will be presented later in this chapter. The optimization procedure was implemented using the PSO toolbox provided by MATLAB.

We aimed to optimize two objective functions: the mean visible transmittance and the mean NIR absorption. We utilized the CWA multi-objective optimization approach discussed previously in chapter 3.2.2 to simultaneously optimize both of these objective functions. We use the following figure of merit (FOM)

$$FOM = w_1 mean(T_{vis}) + w_2 mean(A_{NIR}) \tag{4.1}$$

Where T_{vis} is the transmittance in the visible regime and A_{NIR} is the NIR absorption. w_1 and w_2 are non-negative weights such that

$$w_1 + w_2 = 1 \tag{4.2}$$

The simulation process flow and optimization scheme are illustrated in in Fig. 4.2(a) and 4.2(b) respectively.

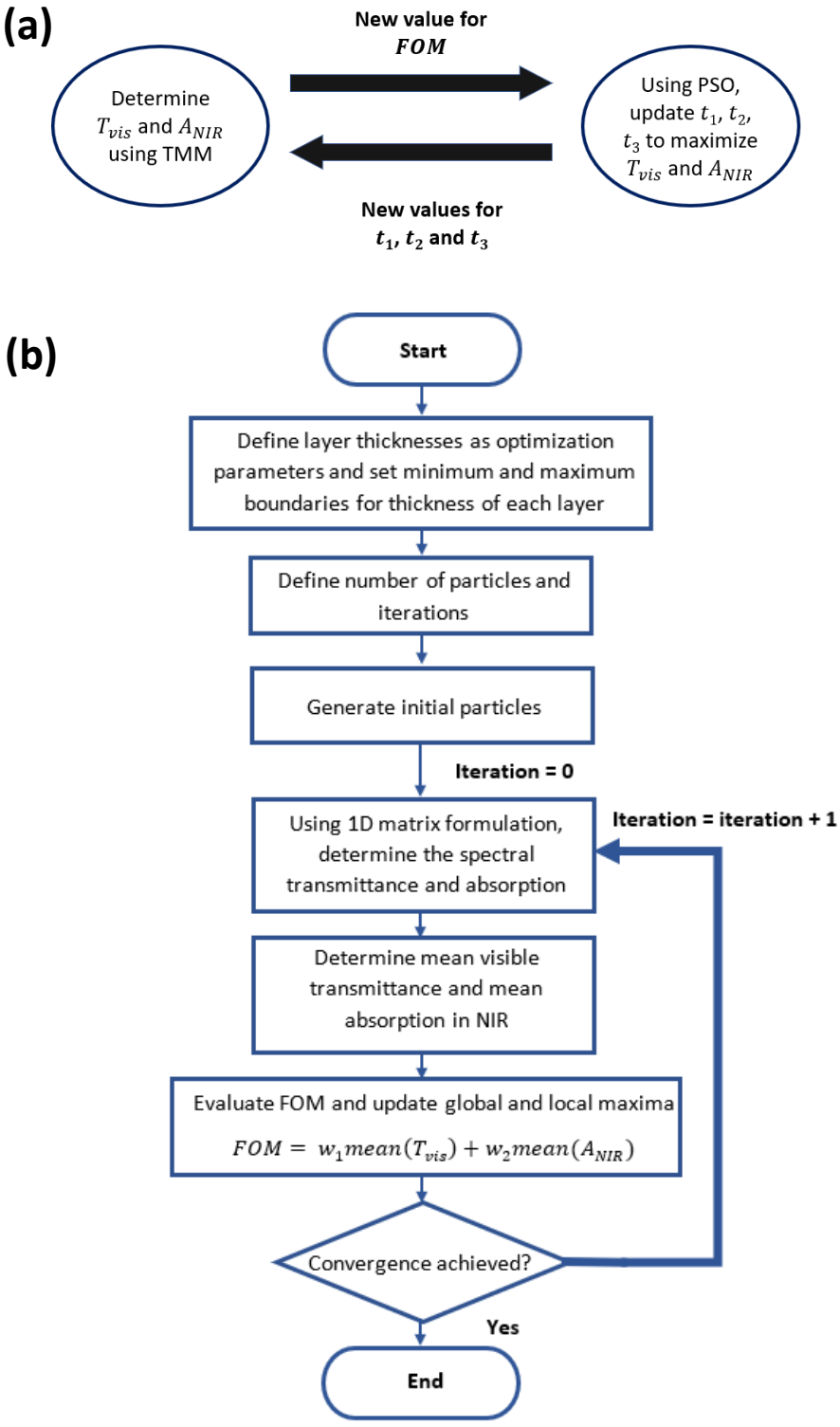

Fig. 4.2: (a) Simulation process flow and (b) optimization scheme.

For the optimization procedure we utilized 15 particles per iteration and carried out 30 iterations running a total of 450 simulations for each material configuration. During optimization, the layer thicknesses were set as the design parameters. The upper and lower bounds set for the thicknesses were 2 nm and 50 nm for the top and bottom layers and 2 nm and 500 nm for the middle SiO_2 spacer.

To determine the values of weights w_1 and w_2 that would give a good trade-off between visible transmittance and NIR absorption, the optimization algorithm was run multiple times for different weight configurations until a good tradeoff between both terms was achieved.

The following approach was taken to decide the values of weights:

1) First the optimization was run for the case when equal weightage was given to visible transmittance term and NIR absorption term (w_1 and w_2 are both 0.5).
2) If the mean visible transmittance dominated over the mean NIR absorption, the value of w_1 was incrementally decreased until a good trade-off between visible transmittance and NIR absorption was found.
3) If the mean NIR absorption dominated over the mean visible transmittance, the value of w_1 was incrementally increased until a good trade-off between visible transmittance and NIR absorption was found.

To illustrate this, for each material configuration investigated, we have tabulated values for absorption (A) and transmittance (T) for different values of w_1 and w_2 in Tables 4.1-4.5. The last column in these tables gives the solar power absorbed by each design under simulated AM 1.5 illumination. This quantity was obtained by first multiplying the absorption profile for each design

with the AM1.5 solar spectrum, followed by integrating the resulting spectra over the 280 nm to 2500 nm wavelength range to calculate the absorbed power density.

Table 4.1: MIM Design 1: Al/SiO_2/Al.

Weight w_1	Weight w_2	t_1 (nm)	t_2 (nm)	t_3 (nm)	Mean visible transmittance	Mean absorption	Absorbed solar power density (W/m^2)
0.5	0.5	2	124	2	0.662	0.230	350.7
0.4	0.6	2	392	2	0.611	0.226	326.7
0.3	**0.7**	**2**	**402**	**3**	**0.523**	**0.259**	**369.4**
0.2	0.8	2	162	4	0.430	0.280	410.2
0.1	0.9	2	178	8	0.192	0.319	442.9

Weight configuration that gives good tradeoff between A and T:

w_1	0.3
w_2	0.7
t_1 (nm)	2
t_2 (nm)	402
t_3 (nm)	3

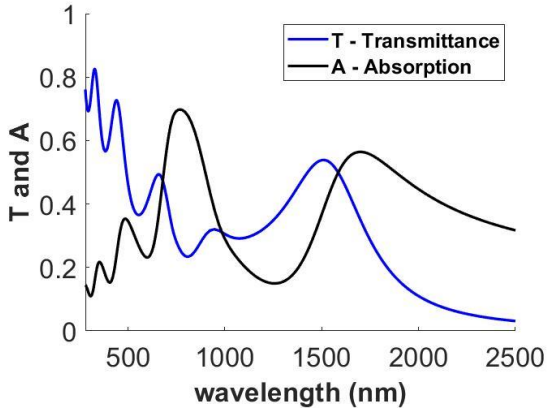

Fig. 4.3: Optical response for Al/SiO_2/Al design in terms of T and A for case when $\boldsymbol{w_1 = 0.3}$ and $\boldsymbol{w_2 = 0.7}$.

Table 4.2: MIM Design 2: Au/SiO_2/Au.

Weight w_1	Weight w_2	t_1 (nm)	t_2 (nm)	t_3 (nm)	Mean visible transmittance	Mean absorption	Absorbed solar power density (W/m^2)
0.5	0.5	2	122	2	0.906	0.134	52.81
0.4	0.6	2	123	2	0.906	0.135	57.78
0.3	0.7	2	126	2	0.905	0.135	52.75
0.2	0.8	2	131	2	0.905	0.135	52.74
0.1	0.9	4	363	7	0.739	0.283	121.4
0.05	0.93	5	392	12	0.605	0.350	157.5
0.04	0.96	5	398	14	0.560	0.367	167.1
0.03	**0.97**	**6**	**404**	**16**	**0.498**	**0.347**	**179.1**
0.02	0.98	7	410	20	0.408	0.375	194.3
0.01	0.99	8	417	26	0.304	0.406	209.5

Weight configuration that gives good tradeoff between A and T:

w_1	0.03
w_2	0.97
t_1 (nm)	6
t_2 (nm)	404
t_3 (nm)	16

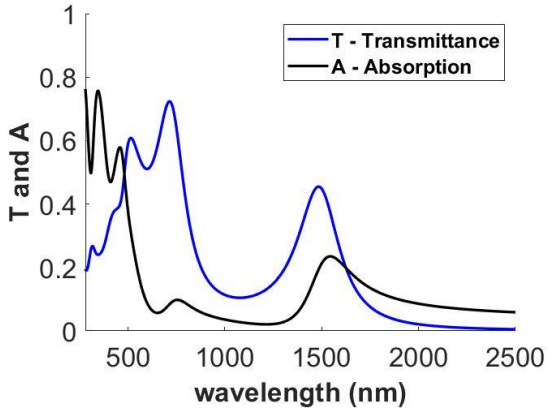

Fig. 4.4: Optical response for Au/SiO_2/Au design in terms of T and A for case when $\boldsymbol{w_1 = 0.03}$ and $\boldsymbol{w_2 = 0.97}$.

Table 4.3: MIM Design 3: $Cu/SiO_2/Cu$.

Weight w_1	Weight w_2	t_1 (nm)	t_2 (nm)	t_3 (nm)	Mean visible transmittance	Mean absorption	Absorbed solar power density (W/m^2)
0.5	0.5	2	127	2	0.859	0.168	103.9
0.4	0.6	2	392	2	0.849	0.168	105.0
0.3	0.7	2	309	2	0.852	0.168	104.4
0.2	0.8	2	162	2	0.850	0.166	104.6
0.1	**0.9**	**4**	**398**	**10**	**0.543**	**0.349**	**253.9**
0.09	0.91	4	403	12	0.490	0.406	270.4
0.08	0.92	5	405	12	0.469	0.418	277.2

Weight configuration that gives good tradeoff between A and T:

w_1	0.1
w_2	0.9
t_1 (nm)	4
t_2 (nm)	398
t_3 (nm)	10

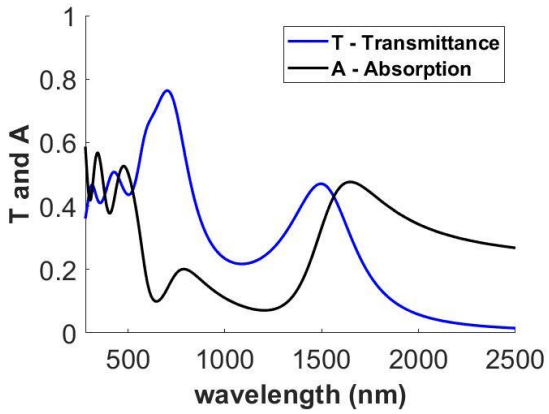

Fig. 4.5: Optical response for $Cu/SiO_2/Cu$ design in terms of T and A for case when $\boldsymbol{w_1 = 0.1}$ and $\boldsymbol{w_2 = 0.9}$.

Table 4.4: MIM Design 4: Ni/SiO_2/Ni.

Weight w_1	Weight w_2	t_1 (nm)	t_2 (nm)	t_3 (nm)	Mean visible transmittance	Mean absorption	Absorbed solar power density (W/m^2)
0.5	0.5	2	143	2	0.719	0.307	322.0
0.49	0.51	3	144	2	0.666	0.358	372.8
0.48	0.52	2	142	2	0.719	0.308	322.3
0.47	**0.53**	**2**	**150**	**6**	**0.530**	**0.475**	**490.0**
0.46	0.54	4	149	6	0.462	0.547	561.8
0.45	0.55	4	150	6	0.469	0.533	556.0
0.44	0.56	3	152	6	0.494	0.517	531.0
0.43	0.57	4	152	7	0.430	0.560	584.3
0.42	0.58	4	151	8	0.401	0.593	605.1
0.41	0.59	4	153	8	0.400	0.593	603.9
0.4	0.6	5	154	8	0.367	0.601	630.0

Weight configuration that gives good tradeoff between A and T:

w_1	0.47
w_2	0.53
t_1 (nm)	2
t_2 (nm)	150
t_3 (nm)	6

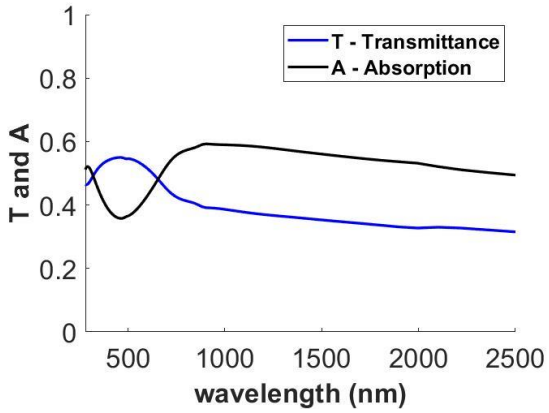

Fig. 4.6: Optical response for Ni/SiO_2/Ni design in terms of T and A for case when $\boldsymbol{w_1 = 0.47}$ and $\boldsymbol{w_2 = 0.53}$.

Table 4.5: MIM Design 5: TiN/SiO_2/TiN.

Weight w_1	Weight w_2	t_1 (nm)	t_2 (nm)	t_3 (nm)	Mean visible transmittance	Mean absorption	Absorbed solar power density (W/m^2)
0.5	0.5	5	154	8	0.618	0.493	491.9
0.51	0.49	5	153	7	0.640	0.466	471.2
0.52	0.48	5	154	7	0.640	0.466	470.9
0.53	0.47	5	154	7	0.640	0.466	470.9
0.54	**0.46**	**5**	**155**	**5**	**0.686**	**0.417**	**421.3**
0.55	0.45	4	156	5	0.715	0.395	390.6
0.56	0.44	5	159	3	0.735	0.355	358.3
0.6	0.4	2	152	4	0.866	0.296	279.3

Weight configuration that gives good tradeoff between A and T:

w_1	0.54
w_2	0.46
t_1 (nm)	5
t_2 (nm)	155
t_3 (nm)	5

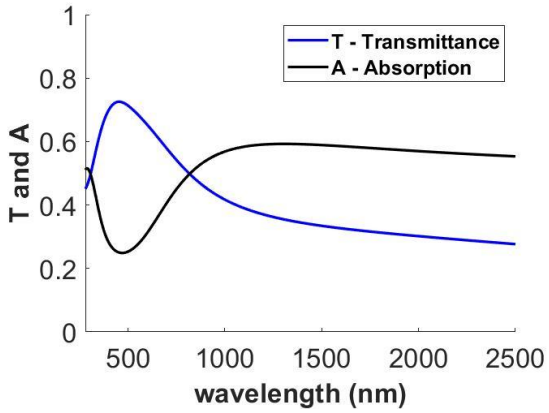

Fig. 4.7: Optical response for TiN/SiO_2/TiN design in terms of T and A for case when $\boldsymbol{w_1 = 0.54}$ and $\boldsymbol{w_2 = 0.46}$.

Table 4.6 summarizes the design details and optical performance for all the optimized designs. Our investigation reveals that cheaper material alternatives perform much better than Au for passive heating applications in case of the MIM geometry. Both the Ni-based and TiN based designs outperform other designs in terms of mean transmittance in the visible region and absorbed solar

power density. Although the former provides lower solar power absorption, the transmission is 15.6% higher for the former compared to the latter. Therefore, we chose the TiN based design for further investigation.

Table 4.6: Summary of layer thicknesses and optical performance for the optimized MIM design for various choices of metals. The dielectric spacer material is SiO_2.

t_1 (nm)	t_2 (nm)	t_3 (nm)	Metal/ Metal nitride	Mean transmittance in visible (400-700 nm)	Maximum transmittance in visible and its location (400-700 nm)	Absorbed solar power density (W/m^2)
2	402	3	Al	0.523	0.727 (441 nm)	369.4
6	404	16	Au	0.498	0.711 (700 nm)	179.1
4	398	10	Cu	0.543	0.763 (700 nm)	253.9
2	150	6	Ni	0.530	0.55 (459 nm)	490.0
5	155	5	TiN	0.686	0.725 (454 nm)	421.3

The analysis presented so far assumed that the spacer material separating the metallic layers is SiO_2. For the case when TiN is taken as the top and bottom layer, we now consider two alternate choices of spacer material: SiN and Al_2O_3. Refractive index data for SiN and Al_2O_3 are taken from [69] and [66] respectively. We reoptimized our designs for these new choices of spacer material. Table 4.7 summarizes the optimized designs and key performance characteristics for three choices of spacer material. The optical response for these three designs from UV to NIR is presented in Fig. 4.8.

Table 4.7: Summary of layer thicknesses and optical performance for the optimized MIM design for various choices of spacer materials. The top and bottom layers of the MIM structure are TiN.

t_1 (nm)	t_2 (nm)	t_3 (nm)	Dielectric spacer	Mean transmittance in visible (400-700 nm)	Maximum transmittance in visible and its location (400-700 nm)	Absorbed solar power density (W/m^2)
5	155	5	SiO_2	0.686	0.725 (454 nm)	421.3
4	114	8	Al_2O_3	0.638	0.683 (445 nm)	441.9
3	95	9	SiN	0.623	0.678 (434 nm)	420.7

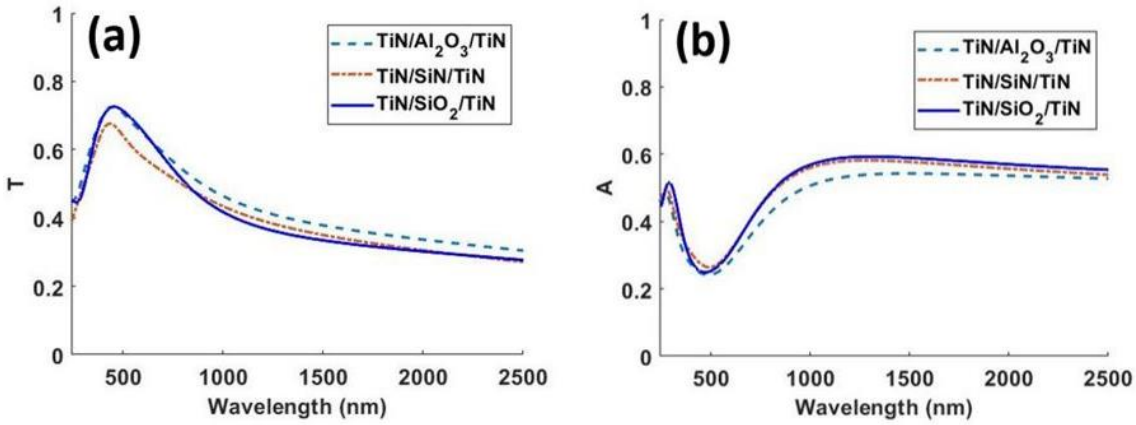

Fig. 4.8: Transmittance 'T' and (b) absorption 'A' spectra for the optimized designs for various choices of spacer materials. For all MIM designs, TiN is used for the top and bottom metal layers.

Among the three choices for spacer materials we considered, the SiN design shows the lowest mean visible transmittance and least solar power absorption. Although the Al_2O_3 design absorbs 20.6 W/m^2 more solar power compared to the SiO_2 design, the latter design shows a significantly higher mean visible transmittance. Therefore, we chose SiO_2 to be the spacer medium for further analysis.

4.2 Enhancing the Performance of the TiN/SiO_2/TiN Design

Our choice of MIM geometry for passive solar heating was motivated by previous reports on the applications of this geometry for the design of perfect absorbers [55-59]. The inverse of this geometry (insulator/metal/insulator or IMI), on the other hand has been used for enhancing transmission of thin film metal layers [20-23, 70, 71]**.** We investigated a combination of MIM and IMI structures to see if such a combination could provide superior performance than what is achievable from MIM alone. As shown in Fig. 4.9(a), the new structure was achieved by adding TiO_2 layers on the two sides of the TiN/SiO_2/TiN structure analyzed in Section 4.1.1. TiO_2 has a higher refractive index than SiO_2 and has high mechanical strength, which makes it a suitable choice for our design [22,70,71].

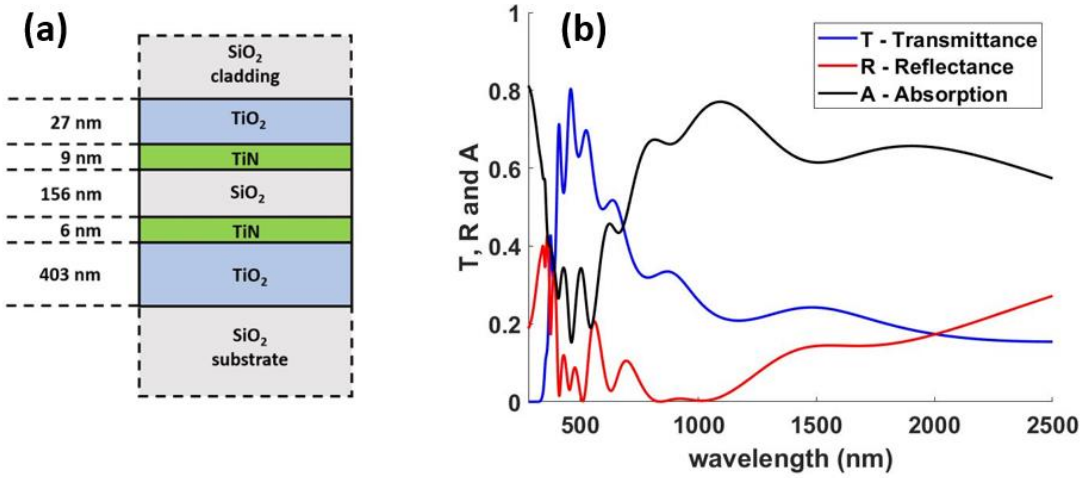

Fig. 4.9: (a) Optimized TiO_2/TiN/SiO_2/TiN/TiO_2 design based on combining MIM and IMI archetecures. (b) optical response of the optimized design.

As done in Section 4.1, transfer matrix formulation in conjunction with PSO was utilized to optimize the layer thicknesses. The upper and lower limits set for the thickness parameter were 2 nm and 50 nm for the TiN layers and 2 nm and 500 nm for the dielectric layer. Addition of two TiO_2 layers increased the complexity of optimization, therefore the total number of particles used

per iteration was increased to 30. 40 iterations were carried out, running a total of 1200 simulations. The optical response of the optimized design is shown in Fig. 4.9(b). A comparison of the optical response before and after addition of the TiO_2 layers to the $TiN/SiO_2/TiN$ design is presented in Table 4.8. We designate the $TiN/SiO_2/TiN$ and the $TiO_2/TiN/SiO_2/TiN/TiO_2$ designs as Design 1 and Design 2 respectively. Although Design 2 has a lower mean visible transmittance compared to Design 1, the addition of TiO_2 layers does enhance the maximum visible transmittance, which reaches values as high as 80%. Furthermore, Design 2 also shows higher solar absorption compared to Design 1

Table 4.8: Summary of optical response for Design 1 and Design 2.

Multilayer design	Mean transmittance in visible (400-700 nm)	Maximum transmittance in visible and its location (400-700 nm)	Absorbed solar power density (W/m^2)
Design 1	0.686	0.725 (454 nm)	421.3
Design 2	0.605	0.803 (459 nm)	508.5

4.3 Investigating Thermal Performance of $TiN/SiO_2/TiN$ and $TiO_2/TiN/SiO_2/TiN/TiO_2$ Designs

In previous sections we have identified two designs which provide good transmission in the visible region, while absorbing a significant amount of solar energy. In this section, we examine the temperature rise achievable when the proposed structures are coated on a glass substrate and exposed to solar radiation. The results presented here are obtained using a combination of Lumerical FDTD and Lumerical HEAT Solver. The process flow showing the procedure carried

out to determine thermal performance of the of our designs is represented in Fig. 4.10. We first carried out 2D FDTD simulations to determine the spatial absorption under normal illumination which is then multiplied by the solar spectrum (AM 1.5) and integrated over the 280 nm to 2500 nm wavelength range to determine the spatial distribution of absorbed power in the xy plane over the area bounded by the dashed yellow lines in Fig. 4.10(b).

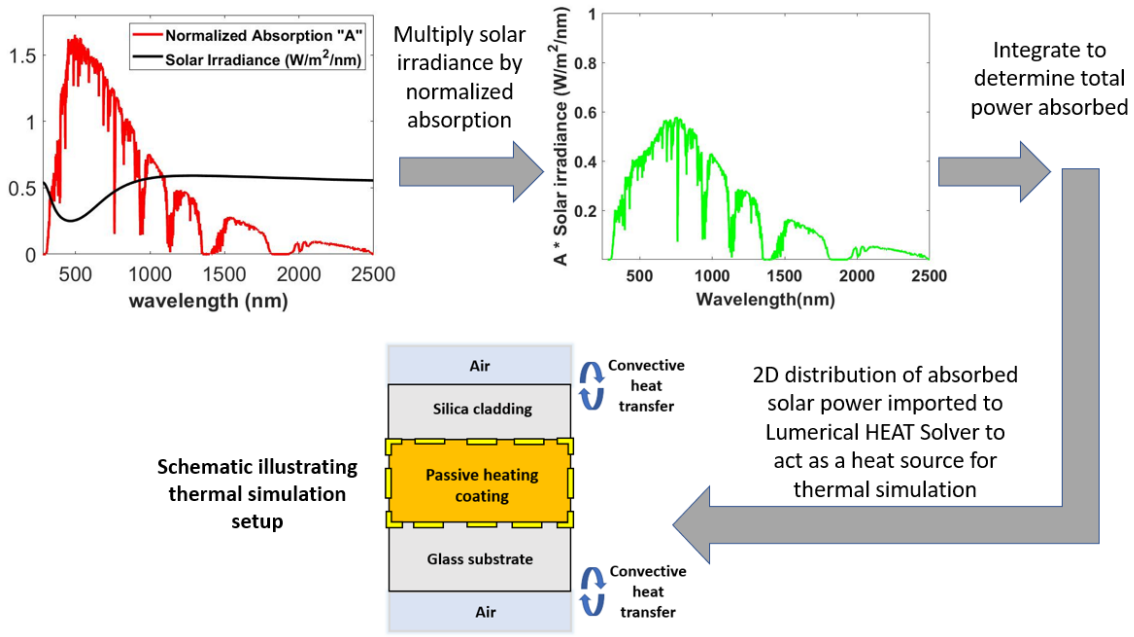

Fig. 4.10: Thermal simulation process flow.

This absorption data was then exported to HEAT. Lumerical does provide a script file for calculating solar absorption, however, after analyzing the code, we found errors which made the script file unsuitable for determining spatial absorption under solar illumination. We modified the script file and verified our code by reproducing results from recent works such as those of [34] and [72]. The corrected FDTD script file is provided in Appendix A.

For thermal simulation in HEAT, the x-span was set to 0.4 μm similar to the one used for FDTD simulation, and the planar multilayer structure was placed on an 0.4 mm thick SiO_2 substrate. A 100 μm SiO_2 coating was applied to the top of the MIM structure to act as a cladding. The ambient temperature of the simulation was kept at 300 K. Convective boundary conditions were applied to the top and bottom of the simulation region to simulate heat dissipation from the device and the heat transfer coefficient was set to 10 $Wm^{-2}K^{-1}$ which is a common value used for air. The thermal simulations predicted that under AM 1.5 solar illumination the steady state temperature of the glass substrate will rise by 21 K and 25 K for Design 1 and 2 respectively.

4.4 Advancing Functionality of Passive Heating Design to Incorporate Thermal Heat Loss Prevention from an Indoor Space

The passive heating designs we have investigated and proposed enable indoor heating by enhancing solar absorption. While these designs provide high absorption of incident solar radiation, they do not prevent long wave thermal radiation from escaping an indoor space. We now advance the functionality of our coating design to incorporate a mechanism of heat loss prevention from a building through reflection of NIR and long wave thermal radiation back inside an indoor space.

In the previous section we discussed IMI architecture enhance transmission of thin film metal layers. As discussed in Chapter 2, low emissivity coatings based on IMI architecture can aid in heat loss prevention from an indoor space through reflection of NIR and/or long wave thermal radiation [20-23, 70, 71]**.** Such coatings allow the possibility of simultaneously achieving both high visible transparency and high reflection of thermal radiation. We now investigate the optical and thermal performance of a passive heating design made through combination of MIM and IMI architecture. The schematic of our proposed design is shown in Fig. 4.11. The left portion of the design that directly faces the sun utilizes an MIM design based on Ni and SiO_2 and functions to maximize

absorption of NIR region of the incident solar radiation. The right portion of the design facing the interior of a building, uses IMI design based on Al and TiO_2 to reflect back light in the near and mid-infrared regime back inside an indoor space.

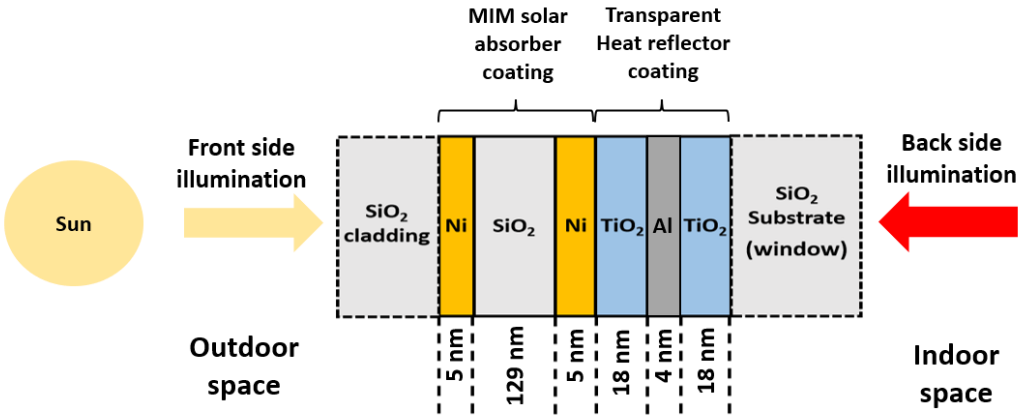

Fig. 4.11: Proposed window coating for maximizing absorption of solar radiation and prevention of heat loss from interior of a building.

The optical response of the design for front side and backside illumination is shows in in Fig. 4.12.

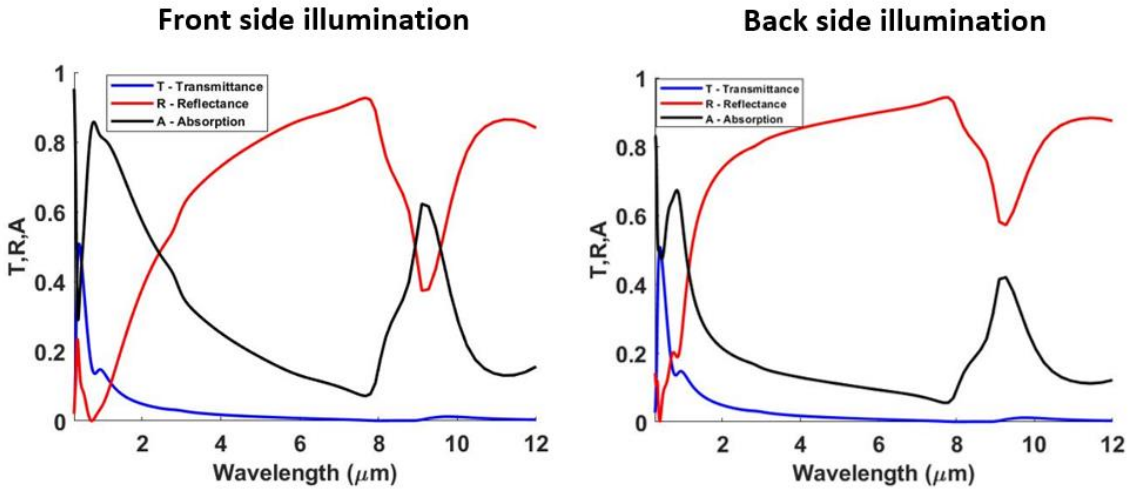

Fig. 4.12: Transmittance (T), reflectance (R) and absorption (A) profiles of the proposed planar multilayer design for (a) front side and (b) backside illumination.

When illuminated from the front side (sunlight illuminating the window), maximum visible transmission exceeds 50% (Fig. 4.12(a)). Thermal simulations showed that under AM 1.5 solar illumination, the coating absorbed 678 W/m^2 of incident solar power. According to Lumerical HEAT simulation, this will result in a temperature rise of the window by 26K. We note that transmission of longer wavelength i.e. heat is close to zero. This is not a major limitation because almost all solar energy reaching earth's surface resides in the visible and near infrared region [9]. When the coating is illuminated by light from the interior (backside illumination in Fig. 4.12(b)), transmission for longer wavelength i.e. heat is extremely low. The transmission in the mid infra-red regime (2.5-12 μm) dropped below 0.05%. Therefore, very little heat will be able to escape the interior.

4.5 Conclusions

In this chapter we examined the applicability of planar multilayer structures for passive heating. We examined two designs. Design 1 is a MIM structure, and the Design 2 is a combination of MIM and IMI. Both of these designs can be implemented using low-cost materials and simple, inexpensive and scalable fabrication process. Our study indicates these design can outperform the more expensive alternative which requires more expensive Au. The planar multilayer designs are not only free of the periodic nano patterning requirements compared to previously reported designs but also outperform previously reported designs in terms of the ability to provide passive heating.

To illustrate this here we compare performance of our designs with two very recent designs [34, 36]. One of the most promising and recent examples of passive heating is [34], which reported 75% overall transmission in the visible spectrum, and 8K rise in temperature under AM 1.5 solar illumination. In contrast, Design 1 and Design 2 demonstrate temperature rise by 21K and 25K

respectively. This higher rise in temperature for our designs comes at the cost of lower overall transmission in the visible spectrum (68.6% for Design 1 and 60.5% for Design 2). Fabrication of the structure reported in [34] requires multiple steps including deposition, etching and lift off. Fabrication of our proposed structure will be considerably simpler since it will require only deposition of multiple layers of thin films. When compared to the asymmetric MIM design recently reported by [36], our Design 1 achieves a higher mean visible transmittance (68.6%) compared to the mean visible transmittance of 60% achieved by [36] while also demonstrating higher mean absorption of 41.7% compared to 36% achieved by [36]. Furthermore, the mean absorption of Design 2 is 16.5% higher than the mean absorption reported by [36] while demonstrating similar mean transmittance values. The proposed passive heating scheme can be adapted to windows for buildings in a number of ways. It can be either deposited directly on a glass window or can be deposited on a transparent polymer coating such as PMMA, which can be attached to a window to achieve passive heating only during winter. It is also possible to integrate this multiplayer structure with commercially available transparent heat reflector window coating technology. Such a window will be able to simultaneously absorb solar energy for passive heating and prevent escape of heat from indoor by reflection, and significantly reduce the heating cost of a building in the cold climate.

Chapter 5

Experimental Demonstration of Transparent Solar Absorbers

From the numerical analysis presented in the previous chapter, we identified several designs with promising optical and thermal performance. In the following we present experimental results to verify our designs. We briefly describe the structures that we fabricated and the process of fabrication. Some measurement results to determine the metal film quality are also presented. We then present results from optical and thermal measurements. Although the observed temperature rise was significant, it was lower than predicted by numerical analysis. We examine some possible reasons behind this discrepancy.

5.1 Designs Chosen for Fabrication

For all our designs, we have chosen low-cost and widely available materials. The only exception was Au which was chosen for its widespread use in previous reports. Our numerical analysis predicted TiN based designs will provide the best performance. Unfortunately, NanoFabrication Kingston (NFK) currently does not have any facility to deposit TiN, but it can deposit Ni, Al and Au. Therefore, we investigated structures that require only those metals. In the previous chapter we have considered two types of designs (MIM and IMIMI), and identified the IMIMI to be better performing. The IMIMI design requires deposition of TiO_2. Although TiO_2 is a widely used dielectric material, currently NFK does not have a process developed for TiO_2 deposition. Therefore, we focused our experimental efforts only on the MIM design. Fig. 5.1 shows the schematic of the structure fabricated. The structure is very similar to the MIM design explored in Chapter 4, with the exception that the top SiO_2 protective layer has not been included.

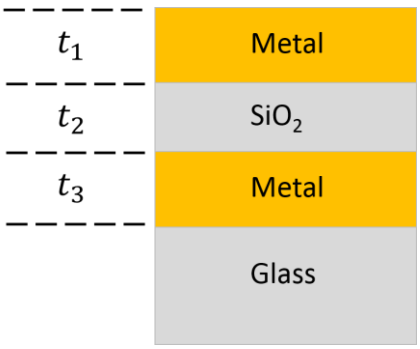

Fig. 5.1: Schematic of MIM design.

Table 5.1 summarizes the dimensions of the structures we fabricated.

Table 5.1: Details of the fabricated samples.

Metal	Sample #	t_1 (nm)	t_2 (nm)	t_3 (nm)
Au	1	16	100	16
	2	6	100	16
Al	3	2	100	3
	4	6	100	6
Ni	5	2	150	6
	6	4	130	4
	7	8	125	8
	8	8	138	8
	9	10	138	10
	10	12	125	12

Although these choices were guided by the optimization carried out in Chapter 4, the dimensions have been altered to some extent for practical reasons. For example, the SiO_2 thicknesses for the Al based design for the fabricated samples are much thinner than the optimized design. This change

has been made to reduce the SiO_2 deposition time. The samples were fabricated in two different time periods. Samples 1,6,7 and 10 were fabricated in June 2021. The rest of the samples were fabricated in November 2021.

We have carried out additional simulations to predict the optical and thermal performance for the structures we fabricated. Table 5.2 summarizes the expected performance for the fabricated samples.

Table 5.2: Simulation results for the fabricated samples.

Metal	Sample #	Mean visible transmittance (400-700 nm)	Absorbed solar power density (W/m^2)	Temperature rise (K)
Au	1	0.403	174.9	9.7
	2	0.557	164.9	9.2
Al	3	0.549	372.9	18.8
	4	0.203	308.0	15.8
Ni	5	0.472	468.9	23.2
	6	0.478	467.4	23.1
	7	0.266	579.6	28.3
	8	0.266	569.6	27.8
	9	0.204	574.9	28.0
	10	0.157	577.1	28.1

Fabrication of our samples started with cleaning of microscope slides, which were used as the substrate. The glass slides were first cleaned in acetone, isopropanol and deionized water. They were then exposed to oxygen plasma in an oxygen plasma cleaning chamber at high power (700

W) to remove any remaining organic material. The cleaning is followed by a three-step thin film deposition process to fabricate the samples described in the previous section. In the first step, a thin metal film is deposited in an electron beam evaporator from Thermionics. A slow deposition rate (1 Å/sec) were used to ensure uniform deposition. The thicknesses of the metal layers deposited were monitored and controlled with the aid of a quartz crystal microbalance.

Deposition of the SiO_2 spacer layer was carried out using RF sputtering system (Lesker PVD 75). The measured SiO_2 thickness is 126.8 nm, as confirmed by profilometry (Fig. 5.2).

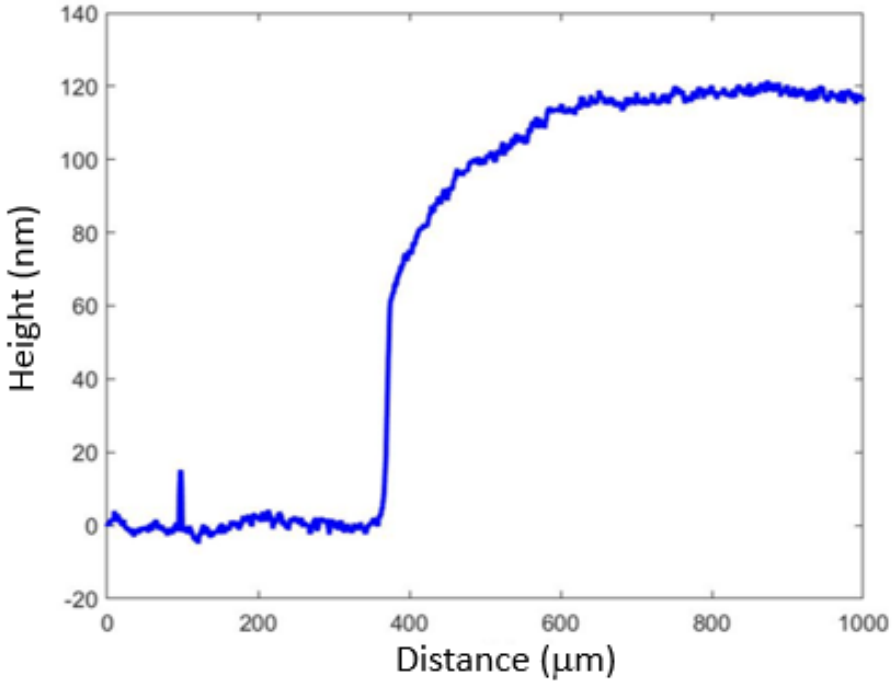

Fig. 5.2: Stylus profilometer measurement of SiO_2 thickness.

The second metal layer was deposited using the same electron beam evaporation process as used for the deposition of the first metal layer. Throughout the fabrication process, each glass slide was partially covered with aluminum foil to allocate a small region of the glass slide where no material

is deposited as shown in Fig 5.3(a). This region of the glass slide would later act as a reference for thermal measurements. The sample after deposition of the first Ni layer is shown in Fig. 5.3(b).

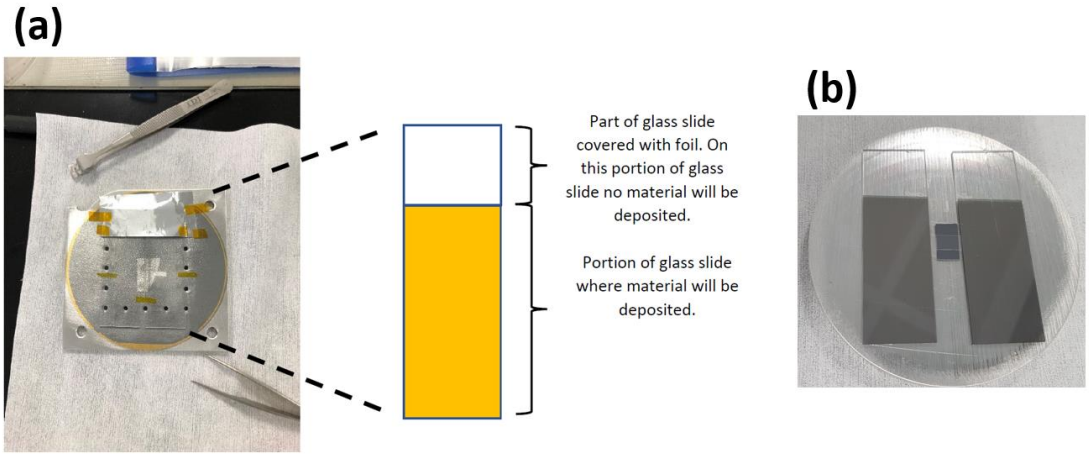

Fig. 5.3: (a) Microscope glass slides partially covered with aluminum foil (b) fabricated sample after deposition of first Ni film layer.

5.2 Optical Characterization

To measure the visible transmittance of our coatings, we conducted spectrophotometry measurements using a DU series 520 spectrophotometer. The transmittance spectra of the samples are presented in Table 5.3. For comparison, we have plotted transmittance predicted by numerical analysis in addition to measurement results in these plots.

Table 5.3: Measured transmission for the fabricated samples.

Device	Mean visible transmittance	Transmission spectrum
16 nm Au/ 100 nm SiO_2/ 16 nm Au Sample #1	0.290 (E) 0.403 (S)	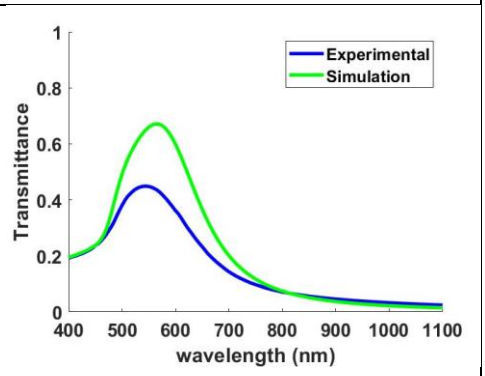
6 nm Au/ 100 nm SiO_2/ 16 nm Au Sample #2	0.293 (E) 0.557 (S)	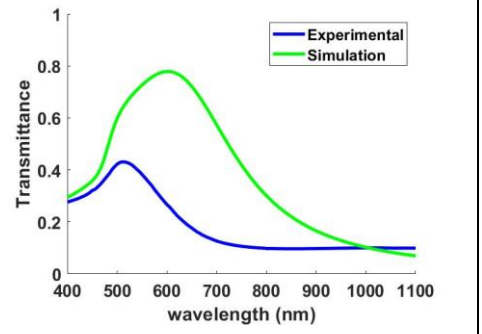
2 nm Al/ 100 nm SiO_2/ 3 nm Al Sample #3	0.967 (E) 0.549 (S)	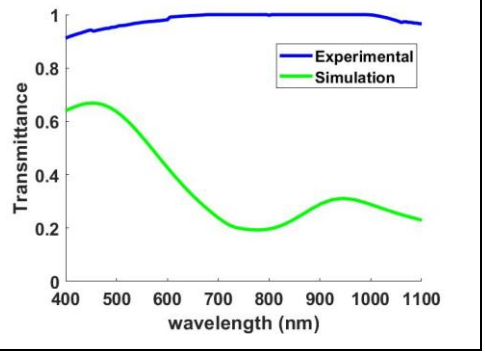

6 nm Al/ 100 nm SiO_2/ 6 nm Al Sample #4	0.494 (E) 0.203 (S)	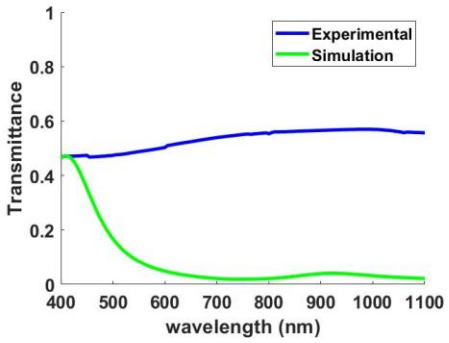
2 nm Ni/ 150 nm SiO_2/ 6 nm Ni Sample #5	0.559 (E) 0.472 (S)	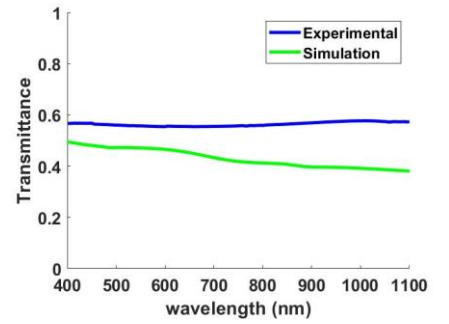
4 nm Ni/ 130 nm SiO_2/ 4 nm Ni Sample #6	0.575 (E) 0.478 (S)	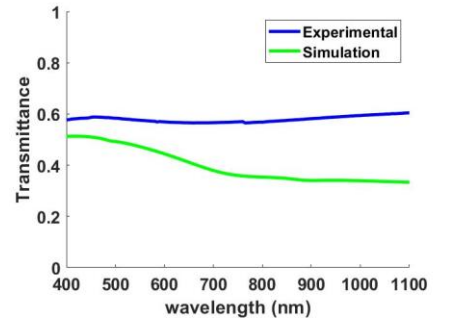
8 nm Ni/ 125 nm SiO_2/ 8 nm Ni Sample #7	0.291 (E) 0.266 (S)	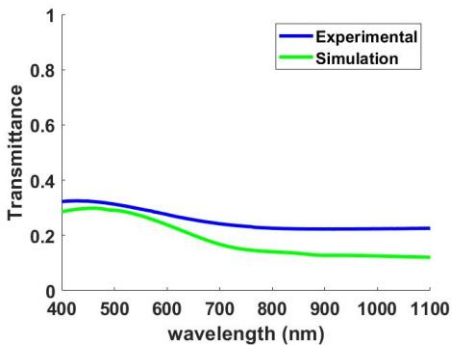

8 nm Ni/ 138 nm SiO_2/ 8 nm Ni Sample #8	0.300 (E) 0.266 (S)	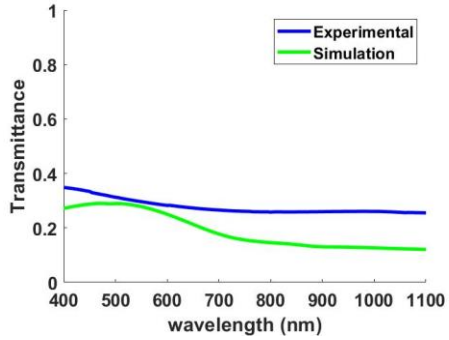
10 nm Ni/ 138 nm SiO_2/ 10 nm Ni Sample #9	0.267 (E) 0.204 (S)	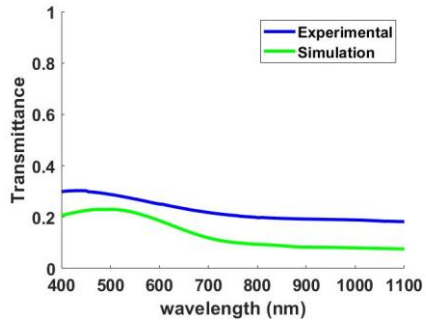
12 nm Ni/ 125 nm SiO_2/ 12 nm Ni Sample #10	0.151 (E) 0.157 (S)	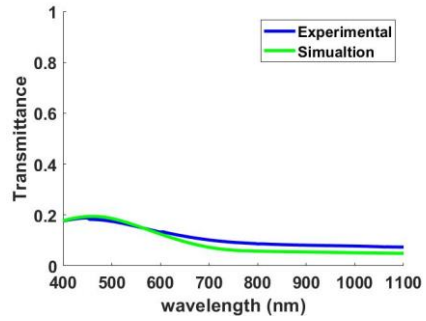

* E: Experimental results, S: Simulation results

To provide a qualitative estimate of what this transmittance means for a viewer inside the building, we have presented photos taken through the samples when they are placed between window and an indoor camera in Fig. 5.4. The outdoor is clearly visible even for moderate transmission.

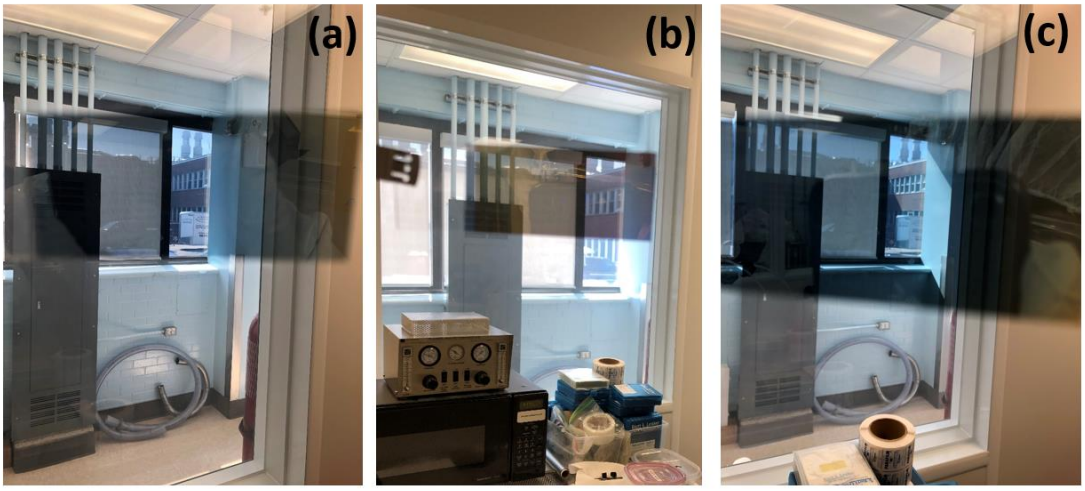

Fig. 5.4: Transmission through (a) 8 nm, (b) 10 nm and (c) 12 nm Ni-based MIM coatings.

Analysis of the results presented in Table 5.3 reveals a few general trends:

a) Experimentally observed transmittance is larger than predicted by numerical analysis (except for the Au samples).
b) Agreement between simulation and measurement becomes better with increasing film thickness.
c) Agreement between simulation and measurement is better in the visible compared to the NIR. region.

Our simulations assume that the metal films are continuous, and the optical properties of these metals are same as those reported in literature. These assumptions are not unreasonable since growth of ultrathin continuous metal films, especially for Ni is well documented in literature [73, 74]. However, growth of ultrathin and continuous metal film is certainly a challenging task. During metal deposition, small grains of metals are deposited on a surface at first and as the film thickness increases, these grains connect with each other and forms a continuous film. In order to understand

the nature of the metal films, we have taken SEM images of various metal films we have deposited. Fig. 5.5 shows the SEM images for Ni films of various thicknesses. It is very difficult to identify the presence of Ni for very small thickness (2 nm) from our SEM image, and the nature of the Ni film remains inconclusive. Grains of Ni are clearly visible for 8 nm thick Ni film. The film becomes almost continuous for the 10 nm thickness.

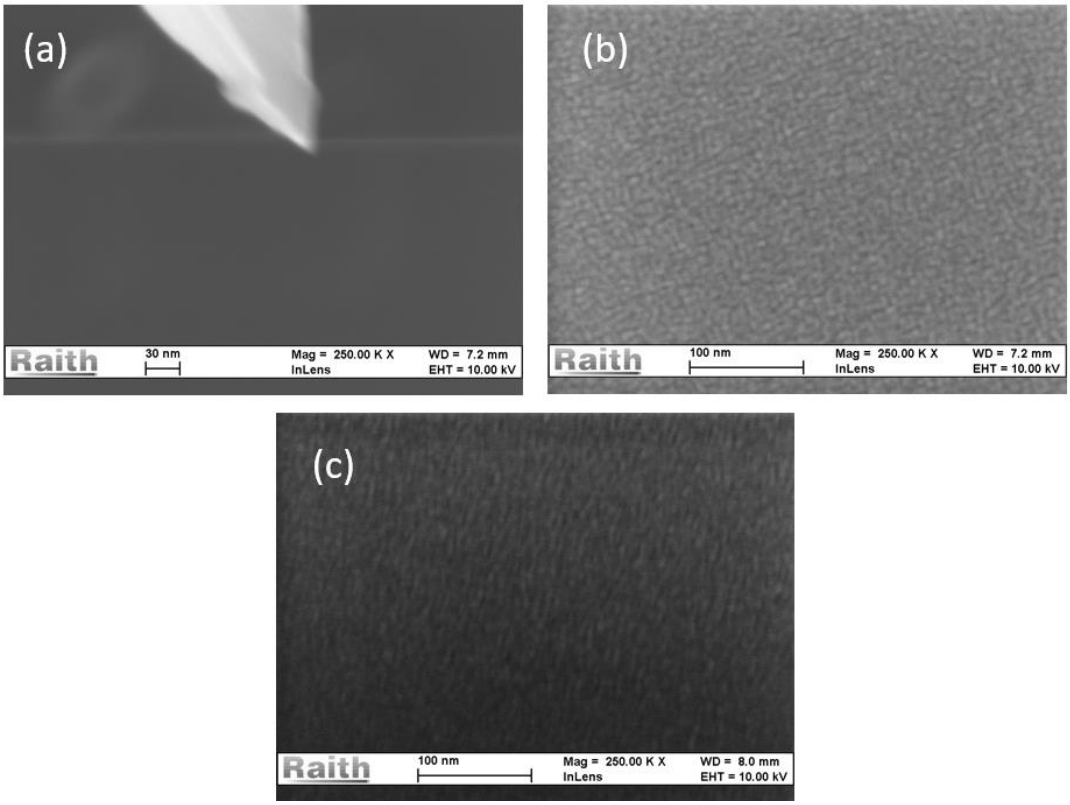

Fig. 5.5: SEM images for Ni film of various thicknesses (a) 2 nm (b) 8 nm (c) 10 nm.

Fig. 5.6 presents SEM images for two different Al film thicknesses. Similar to the case of Ni, the SEM image was not able to provide much information about 2 nm thick Al film. The film becomes nearly continuous for 6 nm thickness.

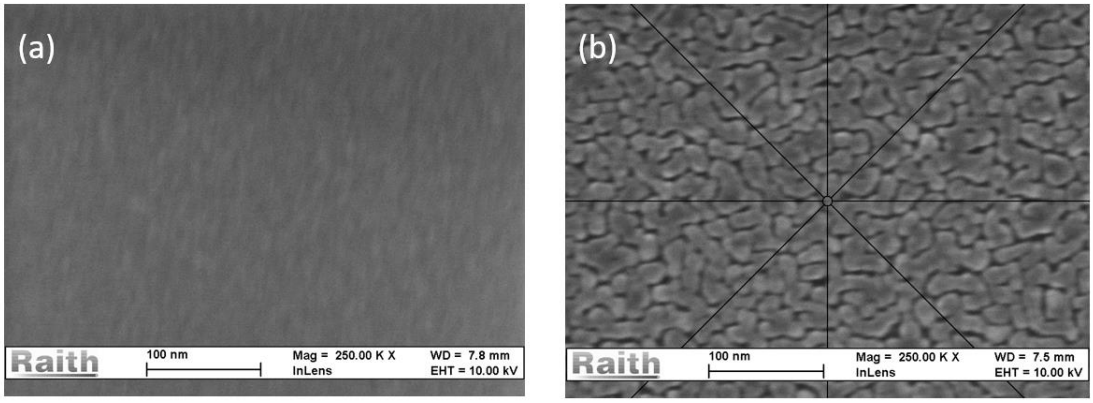

Fig. 5.6: SEM images for Al film of various thicknesses (a) 2 nm (b) 6 nm.

Fig. 5.7 shows the SEM image for a 6 nm thick Au film. Similar to the other cases, large islands of metals are observed, which will form a continuous film for larger thicknesses.

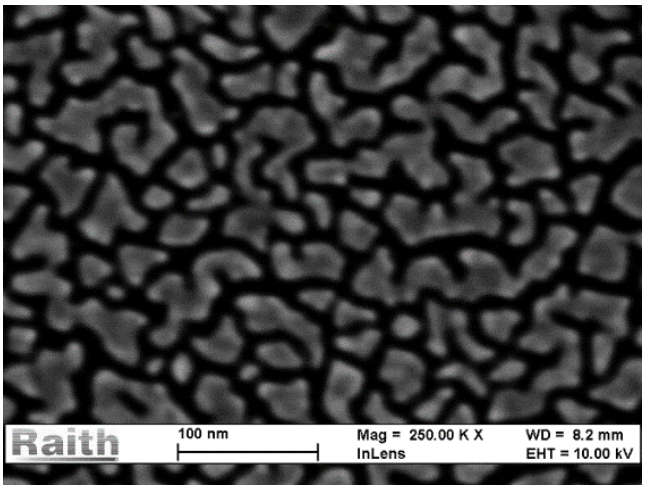

Fig. 5.7: SEM image for 6 nm Au.

To verify if the metal layers in the fabricated samples have the intended thicknesses, we have carried out some AFM measurements. Fig. 5.8(a) shows the two-dimensional AFM scan of a sample for which we attempted to deposit 8 nm thick Ni film on part of a silicon wafer, while the

other part of the wafer was protected from metal deposition. Fig. 5.8(b) shows the thickness profile along the black line shown in Fig. 5.8(a). The film has considerable roughness (RMS: 3.16 nm) and the Ni thickness is roughly 6 nm in contrast to the expected value (8 nm). This may also contribute to the discrepancy observed in the plots presented in Table 5.3.

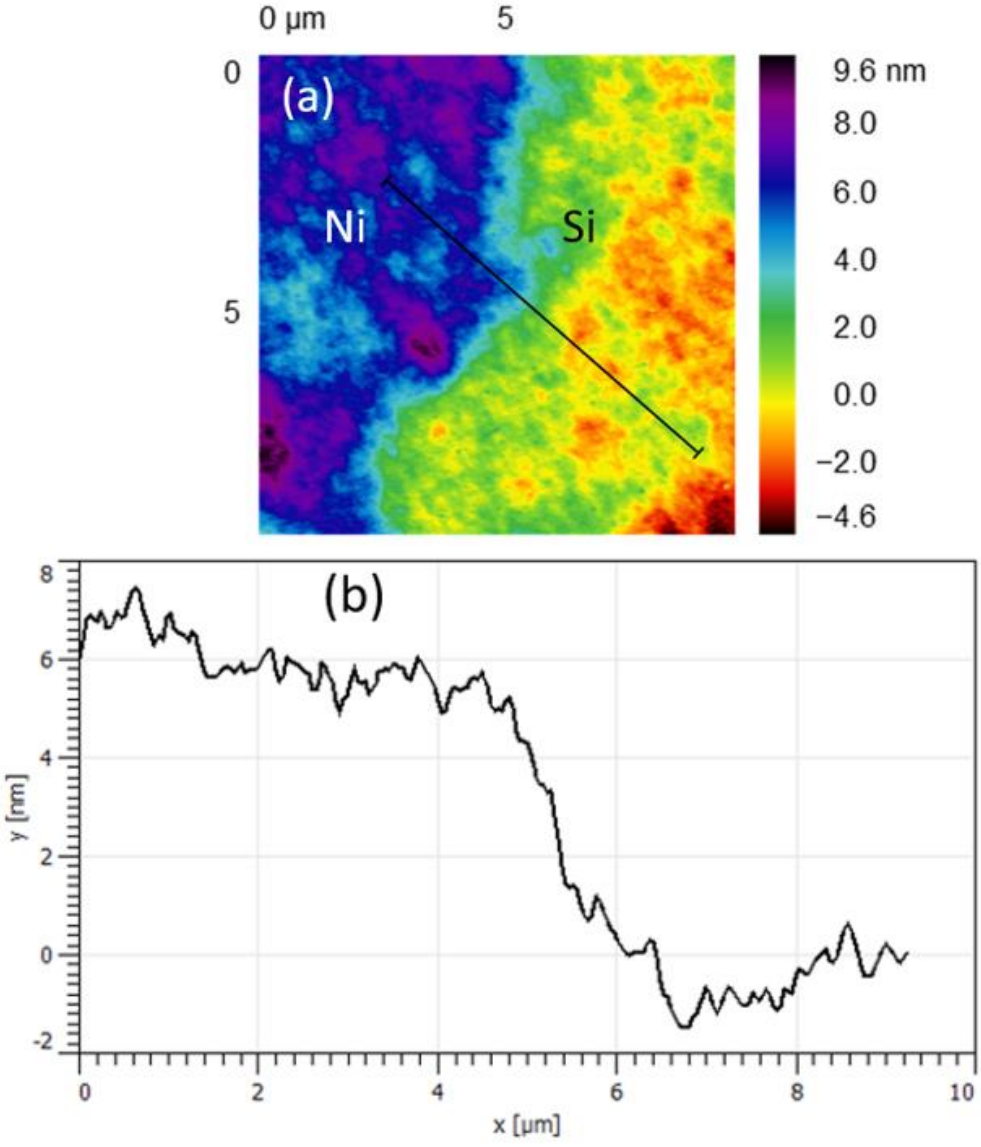

Fig. 5.8: AFM image for 8 nm thick Ni film (a) 2D scan result at the border of the Ni film (b) line plot along the black line in (a).

Another reason behind the discrepancy between simulations and measurements may be the uncertainty in optical properties of metals. Optical properties of dielectric materials are relatively easy to control and the optical properties available from literature are in general reliable for use in numerical analysis. However, the optical properties of metal are highly dependent on the deposition condition and there is a great level of uncertainty regarding suitable choice of optical properties to be used in simulation. This issue was discussed in detail in [75]. Fig. 5.9, which is reproduced from [75] compares the real and imaginary parts of primitivities for Au and Cu reported in various publications, which clearly shows the level of uncertainty one faces while modeling metals in optical designs. Combination of discontinuous nature of the thin metal film, uncertainty in thickness and optical properties of metals used in numerical analysis may be the key reasons behind the discrepancy observed between our modeling and experiment.

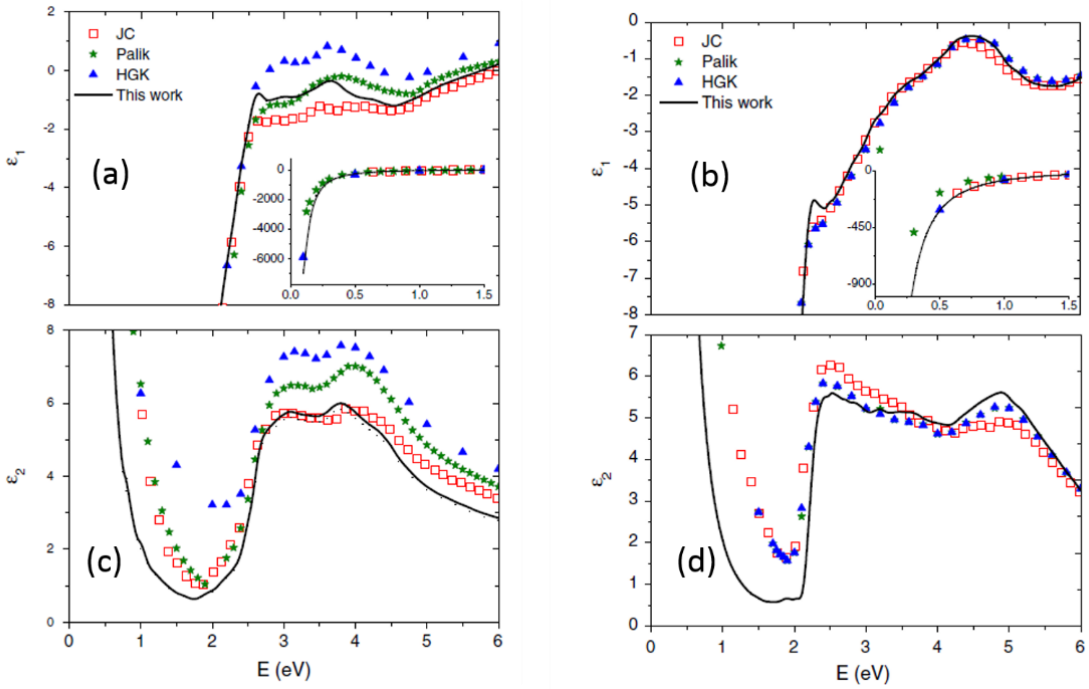

Fig. 5.9: (a) Real and (b) imaginary parts of permittivity of Au. (c) Real and (d) imaginary parts of permittivity of Cu [75].

Long term stability is a major consideration for passive heating scheme. Unlike Au, the less expensive metals, for example, Ni and Al may oxidize when exposed to air, which will affect the performance of the coating. To examine this for our designs, we have repeated transmission measurements for our samples approximately 5 months after the first measurements. Table 5.4 summarizes these results. The results from these two sets of measurements are very similar, which indicates that the samples should be suitable for long term real life applications.

Table 5.4: Long term stability of the fabricated samples.

Sample	Transmission spectrum
Sample #1 16 nm Au/ 100 nm SiO_2/ 16 nm Au	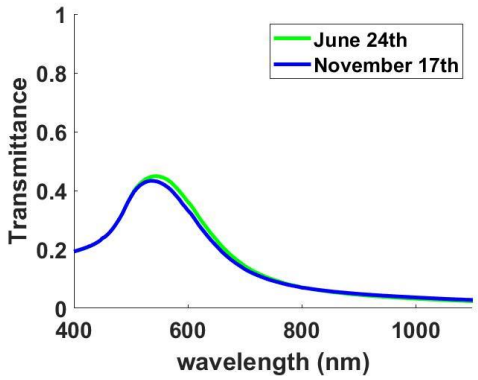
Sample #6 4 nm Ni/ 130 nm SiO_2/ 4 nm Ni	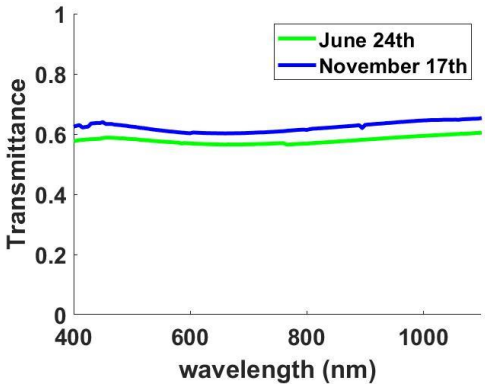

Sample #7 8 nm Ni/ 125 nm SiO_2/ 8 nm Ni	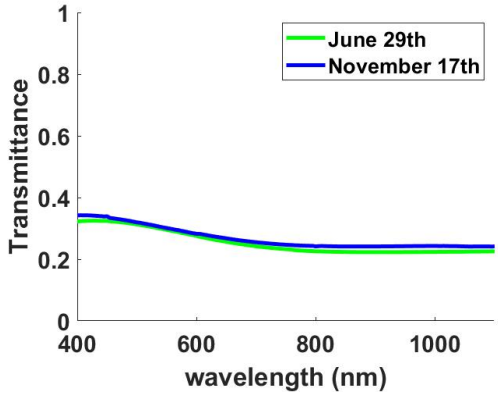
Sample #10 12 nm Ni/ 125 nm SiO_2/ 12 nm Ni	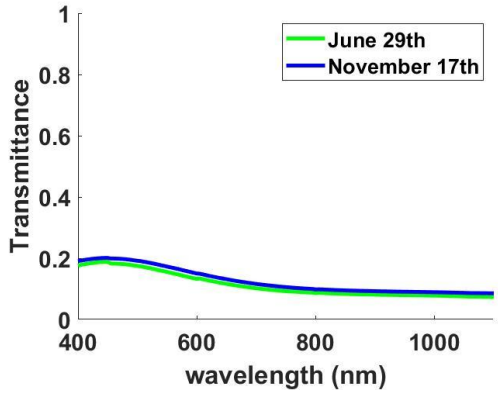

5.3 Thermal Characterization

To analyze the thermal response of the fabricated samples, we investigated the temperature rise achievable when the samples were exposed to direct solar radiation outdoor as well as when samples were illuminated by a solar simulator in a controlled lab setting.

5.3.1 Outdoor Measurements

The schematic of the measurement setup used and a picture of the set up is shown in Fig. 5.10. The samples were kept at an angle of 45° with respect to the ground. This setup allowed us to measure

environmental factors such as humidity and wind speed using an anemometer, as well as variation in solar irradiance incident on the samples using a solar power meter.

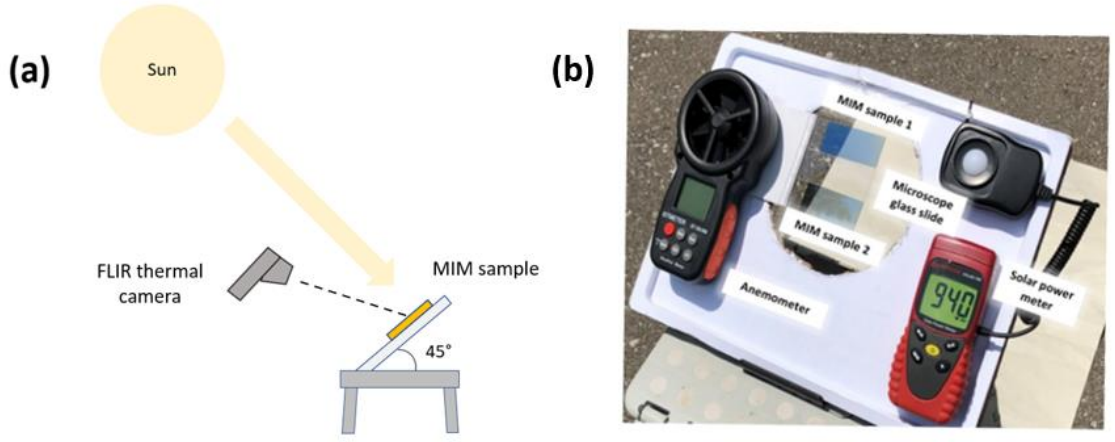

Fig. 5.10: (a) Schematic and (b) photograph of the experimental setup for outdoor thermal measurement.

Thermal tests were conducted during noon on June 2021 for sample 1,6, and 7. Due to cloud coverage, the solar irradiance varied greatly from as low as 293 W/m^2 to as high as 1200 W/m^2. Using a thermal camera (TG-165X by FLIR), temperature readings of the samples and a bare glass side were recorded. As an example of the measurement carried out, values of the environmental parameters for measurements for sample #7 are summarized in Table 5.5. Results from thermal imaging for this measurement are presented in Fig. 5.11. Measurements carried out on sample 1 and 6 are included in Appendix B for reference. For sample #7, a temperature rise of 6.9 K was observed. This was the best result we achieved for outdoor measurements.

Table 5.5: External factors and coating surface temperature rise.

Time of day	12:46 pm
Solar irradiance (W/m^2)	293-1200
Relative humidity (%)	42.7
Wind speed (m/s)	0.3
Coating temperature rise (K)	6.9

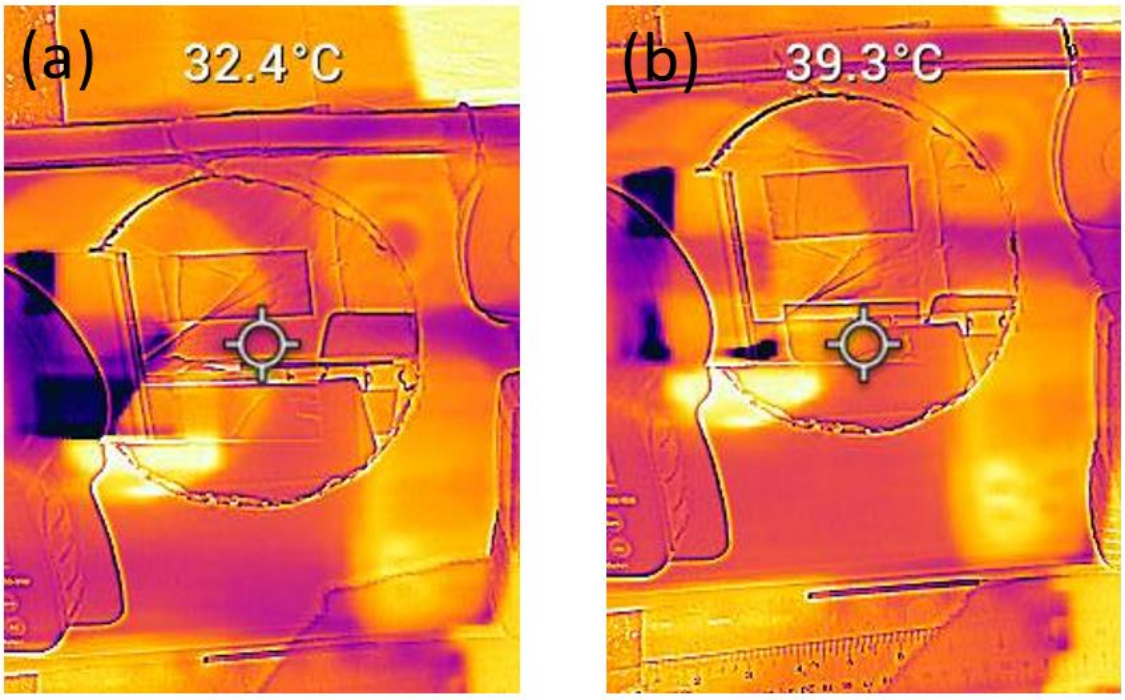

Fig. 5.11: Outdoor temperature measurements for (a) bare glass slide and (b) MIM sample #7 measured under thermal camera crosshair.

5.3.2 Measurements Under Solar Simulator

Additional thermal measurements were carried out in Prof. Karin Hinzer's lab at the University of Ottawa using an Oriel Sol3A solar simulator. The simulator is shown in Fig. 5.12(a) and the experimental setup as shown in Fig. 5.12(b). The sample is placed directly underneath the simulator so that light is normally incident on the sample. An ND filter is placed under the sample such that

very little light returns back to the sample. Therefore, this setup mimics placing the coating on a window.

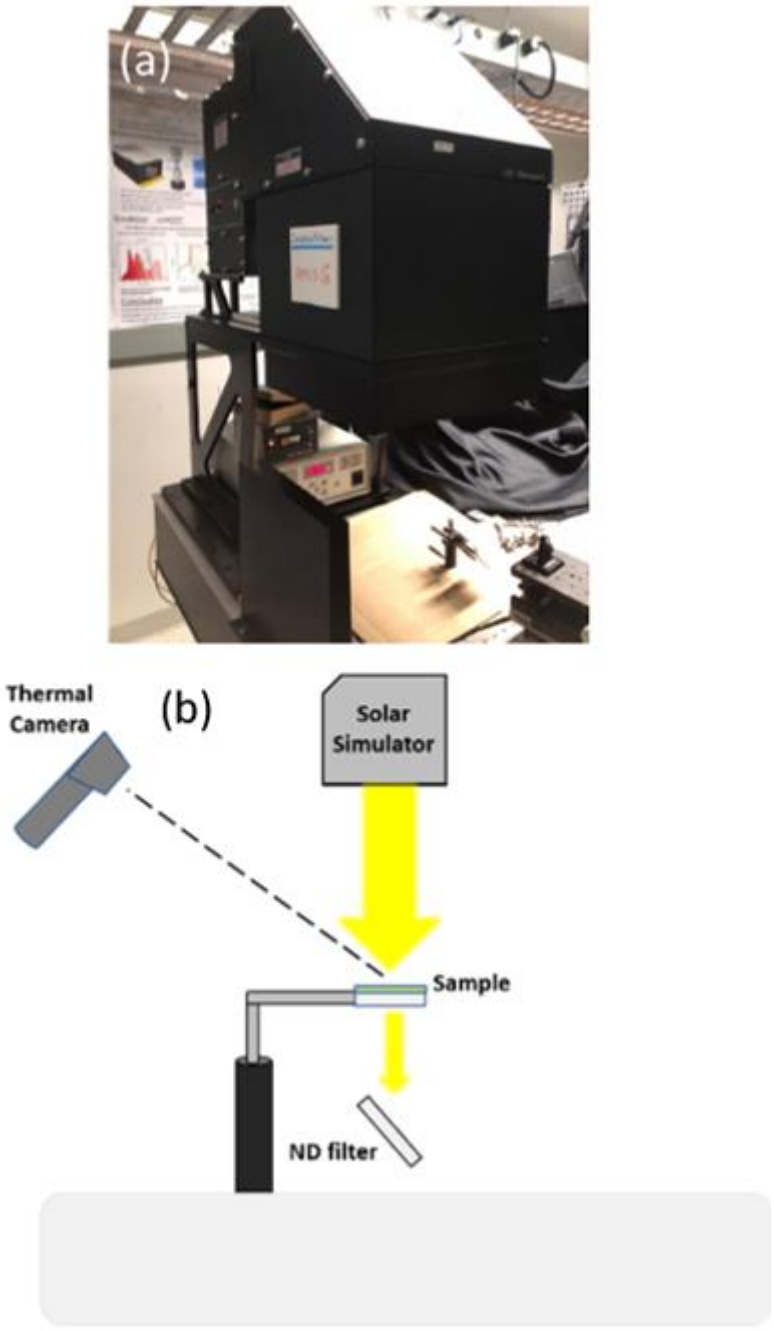

Fig. 5.12: (a) Oriel Sol3A solar simulator (b) experimental setup for thermal measurement.

For thermal measurements, each sample is placed for 5 minutes under the solar simulator to achieve thermal equilibrium. Thermal images were then recorded by the thermal camera. As an example of these measurements, we have shown the thermal images of a bare glass slide and sample #7 in Fig.5.13. The temperature rise observed under the crosshairs of the two images is 3.5 K, which is approximately half of that measured at outdoors (Fig. 5.11). Thermal images for other samples have can be found in Appendix B. The temperature rise observed for the other samples were also lower than that observed during the outdoor measurements. This is not unexpected. The radiation from the solar simulator contains wavelength in the range of 240 nm to 1100 nm, whereas most of the energy of the solar spectrum is distributed from 270 nm to 2500 nm. Since energy from nearly half of solar spectrum is missing in case of the solar radiator, the observed temperature rise is also smaller for measurement under solar simulator.

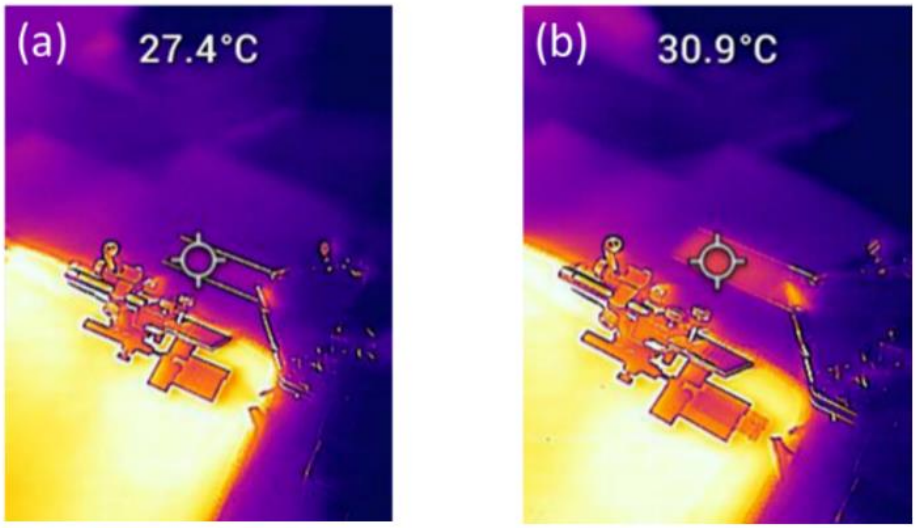

Fig. 5.13: Thermal camera images for (a) bare glass slide (b) MIM sample #7 measured under thermal camera crosshair.

Table 5.6 summarizes the thermal measurement results for all samples.

Table 5.6: Summary of thermal measurements under solar simulator.

Metal	Sample #	t_1 (nm)	t_2 (nm)	t_3 (nm)	Temperature rise (K)
Au	1	16	100	16	0.7
	2	6	100	16	3.3
Al	3	2	100	3	1
	4	6	100	6	5.3
Ni	5	2	150	6	5.6
	6	4	130	4	3.3
	7	8	125	8	3.5
	8	8	138	8	4.9
	9	10	138	10	4.1
	10	12	125	12	1.6

5.4 Conclusion

In this chapter we have presented preliminary experimental results for the designs proposed in the previous chapter. Both optical and thermal measurement data are reported and analyzed. The temperature rise observed was significant but lower than predicted by numerical analysis. Some possible reasons behind this discrepancy have been presented.

Chapter 6

Conclusions and Future Work

6.1 Conclusion

The objective of this thesis was to explore transparent solar absorber window coating designs for passive heating of buildings in cold climate. The main contributions of this thesis are the following:

1) We first carried out investigation regarding the applicability of planar multilayer structures for passive heating of windows. Our analysis reveals that several low cost and widely available materials including Ni and TiN can be better than Au, which has often been used for design of passive transparent coatings in the past. Our thermal simulations indicate that these simple designs may outperform many previous designs which are more expensive and complicated to fabricate in terms of temperature rise under solar illumination.

2) We carried out optical measurements and thermal measurements to verify the results predicted by the numerical analysis. Although the temperature rise was less than predictions from numerical analysis, it was still significant and comparable to recent works done in the field.

3) The benefit of our designs for reduction in energy consumption by modern residential and commercial buildings, where windows form a large part of building surface can be significant. We believe the low-cost, ease of fabrication and ability to provide large

temperature increase under solar illumination may encourage further exploration of multilayer structures for passive heating and cooling applications for many applications.

6.2 Future Work

Further investigation towards improvements of our design, its fabrication and more complete characterization can be undertaken. The quality of the thin metal films can be improved by optimizing the growth process to achieve the large rise in temperature predicted by the numerical analysis. We have carried out experimental investigations for only the MIM design, but IMIMI designs, which should offer better performance, can also be fabricated and tested in the future. Finally, designs with more layers can be investigated in the future to achieve better compromise between transmittance and thermal performance.

References

[1] F. Oldewurtel, A. Parisio, C. N. Jones, D. Gyalistras, M. Gwerder, V. Stauch, B. Lehmann, and M. Morari, “Use of model predictive control and weather forecasts for energy efficient building climate control,” Energy Build., vol. 45, pp. 15–27, 2012.

[2] A. R. Rempel, A. W. Rempel, S. M. McComas, S. Duffey, C. Enright, and S. Mishra, “Magnitude and distribution of the untapped solar space-heating resource in U.S. climates,” Renew. Sustain. Energy Rev., vol. 151, p. 111599, 2021.

[3] World Green Building Council, “Delivering the Paris agreement – The role of the built environment,” https://www.worldgbc.org/sites/default/files/2050%20Letter%20Final_0.pdf

[4] Office for National Statistics, “Excess winter mortality in England and Wales: 2012 to 2013 (provisional) and 2011 to 2012 (final),” https://www.ons.gov.uk/peoplepopulationandcommunity/birthsdeathsandmarriages/deaths/bulletins/excesswintermortalityinenglandandwales/2013-11-26.

[5] Guelph and Wellington Task Force for Poverty Elimination, “Energy poverty,” https://www.gwpoverty.ca/wp-content/uploads/2014/01/Energy-Poverty.pdf.

[6] W. Azeez, “80 million European households struggle to stay warm. Rising energy costs will make the problem worse,” https://www.cnn.com/2021/09/30/business/europe-energypoverty/index.html.

[7] T. M. Boake, “What is sustainable agriculture?,” https://www.tboake.com/2016/125-Passive_design_heating-2016.pdf.

[8] Office of Energy Saver, “Update or replace windows,” https://www.energy.gov/energysaver/update-or-replace-windows.

[9] S. D. Rezaei, S. Shannigrahi, and S. Ramakrishna, “A review of conventional, advanced, and smart glazing technologies and materials for improving indoor environment,” Sol. Energy Mater. Sol. Cells, vol. 159, pp. 26–51, 2017.

[10] D. G. Goswami, Principles of solar engineering, CRC Press, Third Edition, 2015.

[11] N. Ehrmann and R. Reineke-Koch, “Selectively coated high efficiency glazing for solar-thermal flat-plate collectors,” Thin Solid Films, vol. 520, pp. 4214–4218, 2012.

[12] T. Gao and B. P. Jelle, “Silver nanoparticles as low-emissivity coating materials for window glazing applications,” NSTI: Adv., vol. 2, pp. 242–245, 2015.

[13] R. J. Martín-Palma, L. Vázquez, J. M. Martínez-Duart, and Malats-Riera, “Silver-based low-emissivity coatings for architectural windows: Optical and structural properties,” Sol. Energy Mater. Sol. Cells, vol. 53, pp. 55–66, 1998.

[14] J. C. C. Fan and F. J. Bachner, “Transparent heat mirrors for solar-energy applications,” Appl. Opt., vol. 15, p. 1012, 1976.

[15] Vitro Architectural Glass, "The Science of Low-E Coatings," https://glassed.vitroglazings.com/topics/the-science-of-low-e-coatings.

[16] S. Huang, Z. Wang, J. Xu, D. Lu, and T. Yuan, "Determination of optical constants of functional layer of online low-E glass based on the Drude theory," Thin Solid Films, vol. 516, pp. 3179–3183, 2008.

[17] G. K. Dalapati, S. Masudy-Panah, S. T. Chua, M. Sharma, T. I. Wong, H. R. Tan and D. Chi, "Color tunable low cost transparent heat reflector using copper and titanium oxide for energy saving application," Sci. Rep., vol. 6, p. 20182, 2016.

[18] P. Mahtani, K.R. Leong, I. Xiao, A. Chutinan, N.P. Kherani and S. Zukotynski, "Diamond-like carbon based low-emissive coatings," Sol. Energy Mater. Sol. Cells., vol. 95, pp.1630–1637, 2011.

[19] R. Alghamedi, M. Vasiliev, M. Nur-E-Alam, and K. Alameh, "Spectrally-selective all-inorganic scattering luminophores for solar energy-harvesting clear glass windows," Sci. Rep., vol. 4, p. 6632, 2014.

[20] B. E. Yoldas and T. O'Keefe, "Deposition of optically transparent IR reflective coatings on glass," Appl. Opt., vol. 23, p. 3638, 1984.

[21] C. M. Lampert, "Heat mirror coatings for energy conserving windows," Sol. Energy Mater., vol. 6, pp. 1–41, 1981.

[22] M. Okada, M. Tazawa, P. Jin, Y. Yamada, K. Yoshimura, “Fabrication of photocatalytic heat-mirror with TiO2/TiN/TiO2 stacked layer,” Vacuum., vol 80, pp. 732–735, 2006.

[23] B. Karlsson, E. Valkonen, T. Karlsson, and C. G. Ribbing, “Materials for solar-transmitting heat-reflecting coatings,” Thin Solid Films, vol. 86, pp. 91–98, 1981.

[24] C. Chang, M. Liu, L. Pei, G. Chen, Z. Wang, and Y. Ji, “Porous TiNO solar-driven interfacial evaporator for high-efficiency seawater desalination,” AIP Adv., vol. 11, p. 45228, 2021.

[25] C. F. Guo, T. Sun, F. Cao, Q. Liu, and Z. Ren, “Metallic nanostructures for light trapping in energy-harvesting devices,” Light Sci. Appl., vol. 3, p. e161, 2014.

[26] J. Qu, J. Song, J. Qin, Z. Song, W. Zhang, Y. Shi, T. Zhang, H. Zhang, R. Zhang, Z. He, and X. Xue, “Transparent thermal insulation coatings for energy efficient glass windows and curtain walls,” Energy Build., vol. 77, pp. 1–10, 2014.

[27] F. Hu, L. An, C. Li, J. Liu, G. Ma, Y. Hu, Y. Huang, Y. Liu, T. Thundat, and S. Ren, “Transparent and Flexible Thermal Insulation Window Material,” Cell Reports Phys. Sci., vol. 1, p. 100140, 2020.

[28] C-Y. Fan, J-X. Liu, F. Shi, S. Ran, B. Chen, J. Zhou, S. Liu, X. Song and J. Kang, “Facile synthesis of urchin-like Cs x WO 3 particles with improved transparent thermal insulation using bacterial cellulose as a template,” RSC Adv., vol. 9, pp. 5804–5814, 2019.

[29] B. Wang, Q. Wang, Y. Zhu, L. Kang, J. Zhu, F. Jiang, W. Du, D. You, Z. Zhang and F. Gao, “A photo-thermo-dual-responsible CsxWO3/PNIPAM composite hydrogel for energy-efficient windows,” Mater. Res. Express, vol. 6, p. 85708, 2019.

[30] W. Zhong, N. Yu, L. Zhang, Z. Liu, Z. Wang, J. Hu, Z, “Synthesis of CuS nanoplate-containing PDMS film with excellent near-infrared shielding properties,” RSC Adv., vol. 6, pp. 18881–18890, 2016.

[31] D. J. Kim, D. Y. Hwang, J. Y. Park, and H. K. Kim, “Liquid crystal–based flexible smart windows on roll-to-roll slot die–Coated Ag nanowire network films,” J. Alloys Compd., vol. 765, pp. 1090–1098, 2018.

[32] M. Guo, L. Gao, Y. Wei, Y. Ma, Y. Jianyong and B. Ding, “Solar transparent radiators based on in-plane worm-like assemblies of metal nanoparticles,” Sol. Energy Mater. Sol. Cells, vol. 219, p. 110796, 2021.

[33] H. T. Chen, A. J. Taylor, and N. Yu, “A review of metasurfaces: Physics and applications,” Reports Prog. Phys., vol. 79, p. 76401, 2016.

[34] G. Jönsson, D. Tordera, T. Pakizeh, M. Jaysankar, V. Miljkovic, L. Tong, M. P. Jonsson and A. Dmitriev, “Solar transparent radiators by optical nanoantennas,” Nano Lett., vol. 17, pp. 6766–6772, 2017.

[35] R. Ma, D. Wu, Y. Liu, H. Ye, and D. Sutherland, “Copper plasmonic metamaterial glazing for directional thermal energy management,” Mater. Des., vol. 188, p. 108407, 2020.

[36] D. Wu, Y. Meng, and C. Liu, “Design of transparent metasurfaces based on asymmetric nanostructures for directional and selective absorption,” Materials (Basel)., vol. 13, p. 3751, 2020.

[37] E. Mitridis, T. M. Schutzius, A. Sicher, C. U. Hail, H. Eghlidi, and D. Poulikakos, “Metasurfaces leveraging solar energy for icephobicity,” ACS Nano., vol. 12, pp. 7009–7013, 2018.

[38] C. Walker, E. Mitridis, T. Kreiner, H. Eghlidi, T. M. Schutzius, and D. Poulikakos, “Transparent metasurfaces counteracting fogging by harnessing sunlight,” Nano Lett., vol. 19, pp. 1595–1604, 2019.

[39] W. Li, C. Lin, W. Ma, Y. Li, F. Chu, B. Hunag and S. Yao, “Transparent selective photothermal coatings for antifogging applications,” Cell Rep. Phys. Sci., vol. 2, p. 100435, 2021.

[40] A. A. F. Husain, W. Z. W. Hasan, S. Shafie, M. N. Hamidon and S. S. Pandey, “A review of transparent solar photovoltaic technologies,” Renew. Sustain. Energy Rev., vol. 94, pp. 779–791, 2018.

[41] B. P. Jelle and C. Breivik, “The path to the building integrated photovoltaics of tomorrow,” Energy Procedia, vol. 20, pp. 78–87, 2012.

[42] A. P. Raman, M. A. Anoma, L. Zhu, E. Rephaeli and S. Fan, Passive radiative cooling below ambient air temperature under direct sunlight, Nature, vol. 515, p. 540, 2014.

[43] X. Yu, J. Chan and C. Chen, “Review of radiative cooling materials: performance evaluation and design approaches,” Nano Energy, vol. 88, p. 106259, 2021.

[44] C. C. Katsidis and D. I. Siapkas, “General transfer-matrix method for optical multilayer systems with coherent, partially coherent, and incoherent interference,” Appl. Opt., vol. 41, p. 3978, 2002.

[45] H. Kocer, S. Butun, Z. Li, and K. Aydin, “Reduced near-infrared absorption using ultra-thin lossy metals in Fabry-Perot cavities,” Sci. Rep., vol. 5, p. 8157, 2015.

[46] S. Fidanova, “Ant colony optimization,” Stud. Comput. Intell., vol. 947, pp. 3–8, 2021.

[47] R. C. Eberhart and J. Kennedy, “A new optimizer using particle swarm theory,” Proceedings of the Sixth International Symposium on Micro Machine and Human Science, pp. 39-43, 1995.

[48] K. M. Passino, “Biomimicry of bacterial foraging for distributed optimization and control,” IEEE Control Syst., vol. 22, pp. 52–67, 2002.

[49] D. Karaboga and B. Basturk, “Artificial bee colony (ABC) optimization algorithm for solving constrained optimization problems,” Lect. Notes Comput. Sci., vol. 4529, pp. 789–798, 2007.

[50] K. N. Krishnanand and D. Ghose, “Detection of multiple source locations using a glowworm metaphor with applications to collective robotics,” Proceedings - 2005 IEEE Swarm Intelligence Symposium, vol. 2005, pp. 84–91, 2005.

[51] Y. Zhang, S. Wang, and G. Ji, “A Comprehensive Survey on particle swarm optimization algorithm and its applications,” Math. Probl. Eng., vol. 2015, p. 931256, 2015.

[52] A. P. Piotrowski, J. J. Napiorkowski, and A. E. Piotrowska, “Population size in particle swarm optimization,” Swarm Evol. Comput., vol. 58, p. 100718, 2020.

[53] C. A. Coello Coello, G. T. Pulido, and M. S. Lechuga, “Handling multiple objectives with particle swarm optimization,” IEEE Trans. Evol. Comput., vol. 8, pp. 256–279, 2004.

[54] Ansys/Lumerical, “HEAT solver introduction,” https://support.lumerical.com/hc/en-us/articles/360034917713-HEAT-solver-introduction.

[55] K. Takatori, T. Okamoto, K. Ishibashi, “Surface-plasmon-induced ultra-broadband light absorber operating in the visible to infrared range,” Opt. Express., vol. 26, p. 1342, 2018.

[56] D. Huo, J. Zhang, H. Wang, X. Ren, C. Wang, H. Su, H. Zhao, “Broadband perfect absorber with monolayer MoS2 and hexagonal titanium nitride nano-disk array,” Nanoscale Res. Lett., vol. 12, p. 465, 2017.

[57] G. Kenanakis, C.P. Mavidis, E. Vasilaki, N. Katsarakis, M. Kafesaki, E.N. Economou, C.M. Soukoulis, “Perfect absorbers based on metal–insulator–metal structures in the visible region: a simple approach for practical applications,” Appl. Phys. A Mater. Sci. Process., vol. 123, p. 77, 2017.

[58] M. Aalizadeh, A. Khavasi, B. Butun, E. Ozbay, “Large-area, cost-effective, ultra-broadband perfect absorber utilizing manganese in metal-insulator-metal structure,” Sci. Rep., vol. 8, p. 9162, 2018.

[59] A. Ghobadi, H. Hajian, A.R. Rashed, B. Butun, E. Ozbay, “Tuning the metal filling fraction in metal-insulator-metal ultra-broadband perfect absorbers to maximize the absorption bandwidth,”, Photonics Res., vol. 6, p. 168, 2018.

[60] A.K. Chowdhary, T. Bhowmik, J. Gupta, D. Sikdar, “Energy-saving all-weather window based on selective filtering of solar spectral radiation,” Appl. Opt., vol. 60, p. 1315, 2021.

[61] E. Valkonen, B. Karlsson, C.G. Ribbing, “Solar optical properties of thin films of Cu, Ag, Au, Cr, Fe, Co, Ni and Al,” Sol. Energy., vol 32, pp. 211–222, 1984.

[62] M.W. Knight, N.S. King, L. Liu, H.O. Everitt, P. Nordlander, N.J. Halas, “Aluminum for plasmonics,” ACS Nano., vol 8, pp. 834–840, 2014.

[63] A. M. M. Gherman, A. Vladescu, A. E. Kiss, and C. Farcau, “Extraordinary optical transmission through titanium nitride-coated microsphere lattice,” Photonics Nanostructures - Fundam. Appl., vol. 38, p. 100762, 2020.

[64] U. Guler, J. C. Ndukaife, G. V. Naik, A. G. A. Nnanna, A. V. Kildishev, V. M. Shalaev and A. Boltasseva, “Local heating with lithographically fabricated plasmonic titanium nitride nanoparticles,” Nano Lett., vol. 13, pp. 6078–6083, 2013.

[65] W.M. Haynes, CRC handbook of chemistry and physics, CRC press, 2014.

[66] E.D. Palik, Handbook of optical constants of solids, Academic press, 1998.

[67] J. Pflüger, J. Fink, Determination of optical constants by high-energy, electron-energy-loss spectroscopy (EELS), in: E.D.B.T.-H. of O.C. of S. Palik (Ed.), Handb. Opt. Constants Solids, Academic Press, Burlington, 1997.

[68] J. PfÏger, J. Fink, W. Weber, K. P. Bohnen, and G. Crecelius, "Dielectric properties of TiCx, TiNx, VCx, and VNx from 1.5 to 40 eV determined by electron-energy-loss spectroscopy," Phys. Rev. B, vol. 30, pp. 1155–1163, 1984.

[69] K. Luke, Y. Okawachi, M.R.E. Lamont, A.L. Gaeta, M. Lipson, "Broadband mid-infrared frequency comb generation in a Si3N4 microresonator," Opt. Lett., vol. 40, pp. 4823–4826, 2015.

[70] J. Kulczyk-Malecka, P.J. Kelly, G. West, G.C.B. Clarke, J.A. Ridealgh, K.P. Almtoft, A.L. Greer, Z.H. Barber, "Investigation of silver diffusion in TiO2/Ag/TiO2 coatings," Acta Mater., vol. 66, pp. 396–404, 2014.

[71] M. Yuste, R.E. Galindo, S. Carvalho, J.M. Albella, O. Sánchez, "Improving the visible transmittance of low-e titanium nitride based coatings for solar thermal applications," Appl. Surf. Sci., vol. 258, pp. 1784–1788, 2018.

[72] W. Li, Y. Shi, Z. Chen, and S. Fan, "Photonic thermal management of coloured objects," Nat. Commun., vol. 9, p. 4240, 2018.

[73] D. S. Ghosh, "Ultrathin metal transparent electrodes for the optoelectronic industry," PhD Thesis, Universitat Politecnica de Catalunya Barcelona, 2012.

[74] M. L. Grilli, I. D. Sarcina, S. Bossi, A. Rinaldi, L. Pilloni and A. Piegari, “Ultrathin and stable nickel films as transparent conductive electrodes,” Thin Solid Films, vol. 594, pp. 261-265, 2015.

[75] S. Babar and H. Weaver, “Optical constants of Cu, Ag, and Au revisited,” Appl. Opt., vol. 54, pp. 477-481, 2015.

Appendix A

Lumerical Script for Simulation

A.1 FDTD Code for determining absorbed solar power under AM 1.5 illumination

FDTD code used to calculate 2D or 3D spatial solar power absorbed under AM 1.5 illumination and exporting data as a .mat (MAT-file) which can be read by HEAT Solver.

```
##############################################
# Solar power absorbed

f=getdata("field","f");
x=getdata("field","x",1);
y=getdata("field","y",1);
z=getdata("field","z",1);
delta_x=getdata("field","delta_x",1);
delta_y=getdata("field","delta_y",1);
if (havedata("field","dimension")==3) {
delta_z=getdata("field","delta_z",1);
} else {
delta_z = 0;
}

Nx = length(x);
Ny = length(y);
Nz = length(z);
Nf = length(f);

##############################################################################
##

# Get the AM1.5 solar spectrum
lam_nm = solar(0)*1e9; # solar spectrum wavelength vector, in units of nm.
Psolar = solar(1)*1e-9; # solar power spectrum, in units of Watts/m^2/nm
f_solar = 1e9*c/lam_nm; # solar spectrum frequency vector, in units of Hz
Nf_solar = length(f_solar);

# select the region of solar spectrum covered by the monitor data
fl = max([min(f_solar),min(f)]);
```

```
fh = min([max(f_solar),max(f)]);
fi = find((f_solar>=fl)&(f_solar<=fh));
f_solar = f_solar(fi);
lam_nm = lam_nm(fi);
Psolar = Psolar(fi);
Nf_solar = length(f_solar);
nm = Psolar * source_area; # solar power in W at every frequency point (W/nm)

nm = meshgrid4d(4,x,y,z,nm);

W = meshgrid4d(4,x,y,z,f*2*pi); # create 4D matrix of f
SP = meshgrid4d(4,x,y,z,sourcepower(f_solar)); # 4D matrix of source power

# calculate spatial absorption again from each field component separately (watts/m^3)
if (havedata("index","index_x")) {
Pabs_x =
0.5*eps0*W*(abs(getdata("field","Ex",1))^2*imag(getdata("index","index_x",1)^2));
Pabs_y =
0.5*eps0*W*(abs(getdata("field","Ey",1))^2*imag(getdata("index","index_y",1)^2));
} else {
Pabs_x = matrix(Nx,Ny,Nz,Nf);
Pabs_y = matrix(Nx,Ny,Nz,Nf);
}
if (havedata("index","index_z")) {
Pabs_z =
0.5*eps0*W*(abs(getdata("field","Ez",1))^2*imag(getdata("index","index_z",1)^2));
} else {
Pabs_z = matrix(Nx,Ny,Nz,Nf);
}

# spatially interpolate absorption to standard mesh cell locations
Pabs_matrix = ( interp(Pabs_x,x+delta_x,y,z,f,x,y,z,f_solar) +
interp(Pabs_y,x,y+delta_y,z,f,x,y,z,f_solar) +
interp(Pabs_z,x,y,z+delta_z,f,x,y,z,f_solar) ) / SP;
Pabs_x=0; Pabs_y=0; Pabs_z=0; W=0; SP=0; # Clear variables to free memory
# end absorption calculation

# Calculate the power absorbed under solar illumination

E_thermal_total = nm * Pabs_matrix; # total power absorbed W/m^3/nm
Pheat_matrix = integrate2(E_thermal_total,4,lam_nm);

# end power absorbed cal

##############################################################
# unfold data if symmetry BC's were used.
```

```
?"Unfolding";
if ( (length(getdata("field","x",1)) != length(getdata("field","x",2))) ) {
xTemp = x;
x = [-x(Nx:-1:2); x];
PabsTemp = Pabs_matrix;
Pabs_matrix = matrix(2*Nx-1,Ny,Nz,Nf);
PheatTemp = Pheat_matrix;
Pheat_matrix = matrix(2*Nx-1,Ny,Nz);
Pabs_matrix(1:(Nx-1),1:Ny,1:Nz,1:Nf) = PabsTemp(Nx:-1:2,1:Ny,1:Nz,1:Nf);
Pabs_matrix(Nx:(2*Nx-1),1:Ny,1:Nz,1:Nf) = PabsTemp;
Pheat_matrix(1:(Nx-1),1:Ny,1:Nz) = PheatTemp(Nx:-1:2,1:Ny,1:Nz);
Pheat_matrix(Nx:(2*Nx-1),1:Ny,1:Nz) = PheatTemp;
Nx = length(x);
}
if (length(getdata("field","y",1)) != length(getdata("field","y",2))) {
yTemp = y;
y = [-y(Ny:-1:2); y];
PabsTemp = Pabs_matrix;
Pabs_matrix = matrix(Nx,2*Ny-1,Nz,Nf);
Pabs_matrix(1:Nx,1:(Ny-1),1:Nz,1:Nf) = PabsTemp(1:Nx,Ny:-1:2,1:Nz,1:Nf);
Pabs_matrix(1:Nx,Ny:(2*Ny-1),1:Nz,1:Nf) = PabsTemp;
Pheat_matrix(1:Nx,1:(Ny-1),1:Nz) = PheatTemp(1:Nx,Ny:-1:2,1:Nz);
Pheat_matrix(1:Nx,Ny:(2*Ny-1),1:Nz) = PheatTemp;
Ny = length(y);
}
PabsTemp=0; PheatTemp=0; # Clear memory
# end of unfolding

############################################################
# Export data to DEVICE. Compress data in 3rd dimension, and Array the generation rate
'periods' time

# check inputs
dim = getdata("field","dimension");
if ((%average dimension% != "x") & (%average dimension% != "y")) { %average
dimension% = "none"; }
if ( periods < 1 ) { periods=1; }
if ( (dim==2) & (%average dimension% != "none") ) { message("Warning! Should not
average in 2D simulations."); }

# average data over 3rd dimension for export to DEVICE
if (%average dimension% == "x") {
Pheat_temp = matrix(2,Ny,Nz);
Pheat_temp(1,1:Ny,1:Nz) = integrate2(Pheat_matrix,1,x)/(max(x)-min(x));
Pheat_temp(2,1:Ny,1:Nz) = integrate2(Pheat_matrix,1,x)/(max(x)-min(x));
x_export = [min(x), max(x)];
```

```
Pheat_matrix_export = Pheat_temp;
y_export = y;
z_export = z;
}
if (%average dimension% == "y") {
Pheat_temp = matrix(Nx,2,Nz);
Pheat_temp(1:Nx,1,1:Nz) = integrate2(Pheat_matrix,2,y)/(max(y)-min(y));
Pheat_temp(1:Nx,2,1:Nz) = integrate2(Pheat_matrix,2,y)/(max(y)-min(y));
y_export = [min(y), max(y)];
Pheat_matrix_export = Pheat_temp;
x_export = x;
z_export = z;
}
if ((dim==3) & (%average dimension% == "none")) {
Pheat_matrix_export = Pheat_matrix;
x_export = x;
y_export = y;
z_export = z;
}
if ((dim==2) & (%average dimension% == "none")) {
Pheat_matrix_export = matrix(Nx,Ny,2);
Pheat_matrix_export(1:Nx,1:Ny,1) = Pheat_matrix;
Pheat_matrix_export(1:Nx,1:Ny,2) = Pheat_matrix;
x_export = x;
y_export = y;
z_export = [-1e-6,1e-6];
Nz=2;
}
# array data to include multiple periods for export to DEVICE.
if ( (%average dimension% == "x") & (periods>1) ) {
Ptemp = Pheat_matrix_export;
for(i=1;i<periods;i=i+1){
Pheat_matrix_export = [Pheat_matrix_export, Ptemp(1:length(x_export),2:Ny,1:Nz)];
y_export = [y_export; y(2:Ny)+max(y_export)-min(y_export)];
}
y_export = y_export - (max(y_export) + min(y_export))/2; # re-center at zero
}
if ( ((%average dimension%=="none") | (%average dimension%=="y")) & (periods>1) )
{ # for 3D and 2D, stretch in x direction only
Ptemp = Pheat_matrix_export;
for(i=1;i<periods;i=i+1){
Pheat_matrix_export = [Pheat_matrix_export; Ptemp(2:Nx,1:length(y_export),1:Nz)];
x_export = [x_export; x(2:Nx)+max(x_export)-min(x_export)];
}
x_export = x_export - (max(x_export) + min(x_export))/2; # re-center at zero
}
```

```
temp=0;

# Use proper variable name for export to DEVICE data file.
# create backup copy of original data
x_original=x;
y_original=y;
z_original=z;
x=x_export;
y=y_export;
z=z_export;
Pabs_thermal = rectilineardataset("Pabs_thermal",x,y,z);
Pabs_thermal.addattribute("Pabs_thermal",Pheat_matrix_export); # watt/m^3

if(length(%Q export filename%)>0){
?"save data file for DEVICE";
matlabsave(%Q export filename%,Pabs_thermal);
}
# revert back to standard position vectors
x = x_original;
y = y_original;
z = z_original;
Nz=length(z);

# create data sets
Pabs = rectilineardataset("Pabs",x,y,z);
Pabs.addparameter("lambda",c/f_solar,"f",f_solar);
Pabs.addattribute("Pabs",Pabs_matrix);

Pabs_thermal_export = Pabs_thermal;

Pabs_thermal = rectilineardataset("Pabs_thermal",x,y,z);
Pabs_thermal.addattribute("Pabs_thermal",Pheat_matrix); # watt/m^3

Pabs_total = matrixdataset("Pabs total");
Pabs_total.addparameter("lambda",c/f_solar,"f",f_solar);
Pabs_total.addattribute("Pabs_total",integrate2(Pabs_matrix,1:3,x,y,z));
Pabs_total.addattribute("Pabs_thermal_total",interp(integrate2(E_thermal_total,1:3,x,y,z)
,f_solar,f_solar) ); # watt/nm
```

Appendix B

Thermal Measurements Under Outdoor and Controlled Lab Setting

B.1 Thermal Measurements Under Outdoor Conditions

Table B.1: External factors and coating surface temperature rise for sample #1.

Time of day	2:01 pm
Solar irradiance (W/m^2)	1040-1060
Relative humidity (%)	22.7
Wind speed (m/s)	0.3
Coating temperature rise (K)	3.8

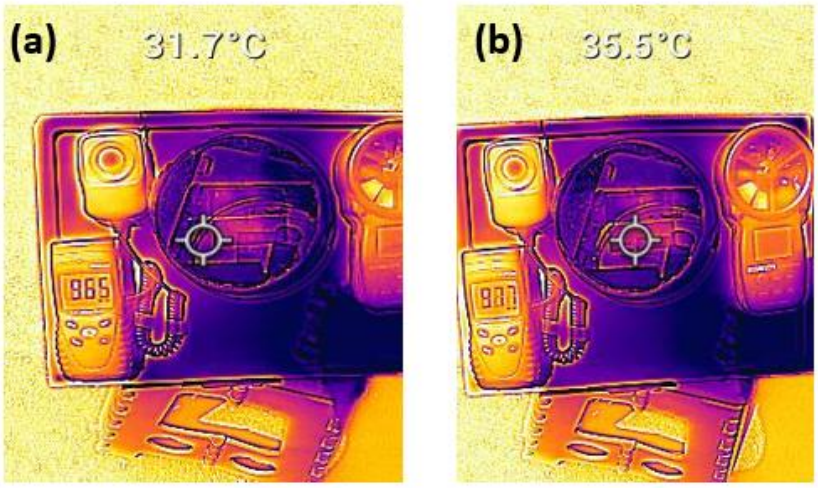

Fig. B.1: Outdoor temperature measurements for (a) bare glass and (b) MIM sample #1 measured under thermal camera crosshair.

Table B.2: External factors and coating surface temperature rise for sample #6.

Time of day	2:25 pm
Solar irradiance (W/m^2)	736-916
Relative humidity (%)	22.7
Wind speed (m/s)	0.3
Coating temperature rise (K)	5.4

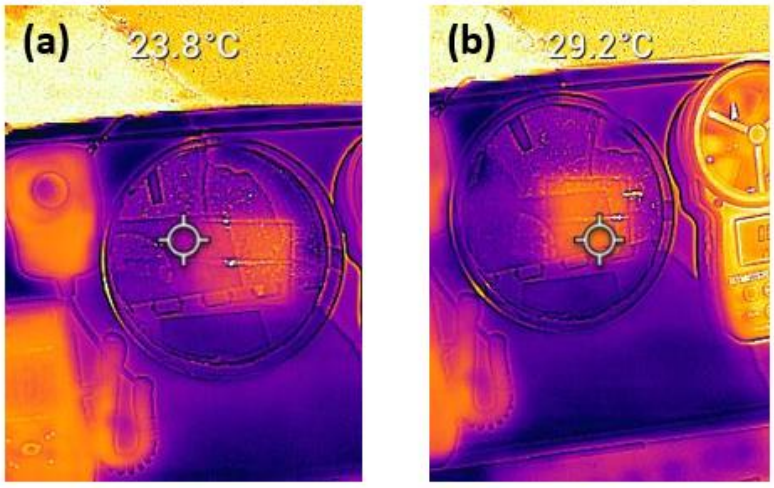

Fig. B.2: Outdoor temperature measurements for (a) bare glass and (b) MIM sample #6 measured under thermal camera crosshair.

B.2 Thermal Measurements Under Controlled Lab Setting

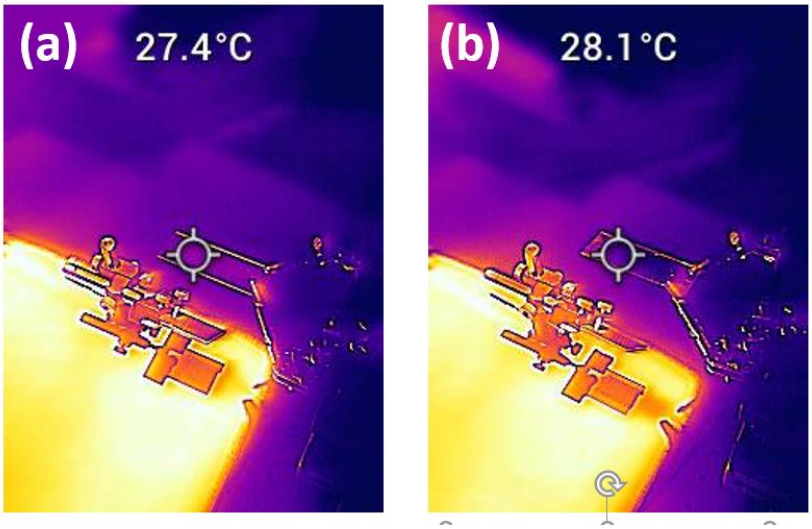

Fig. B.3: Thermal camera images for (a) bare glass slide (b) MIM sample #1 measured under thermal camera crosshair.

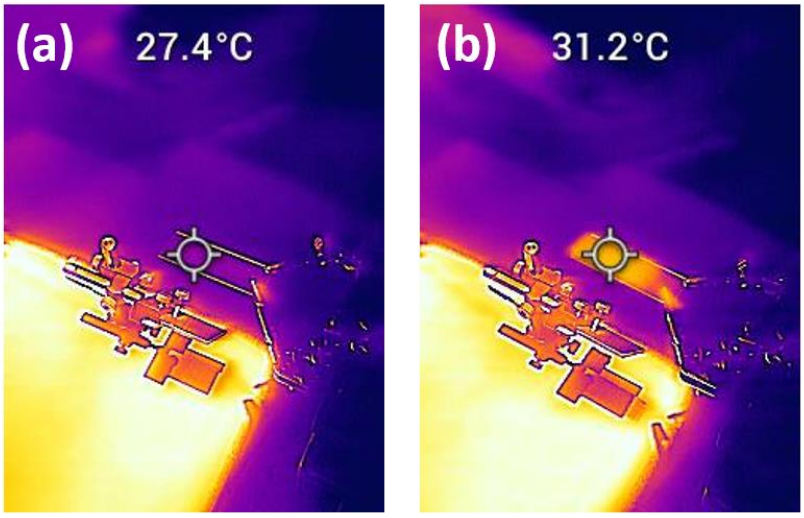

Fig. B.4: Thermal camera images for (a) bare glass slide (b) MIM sample #2 measured under thermal camera crosshair.

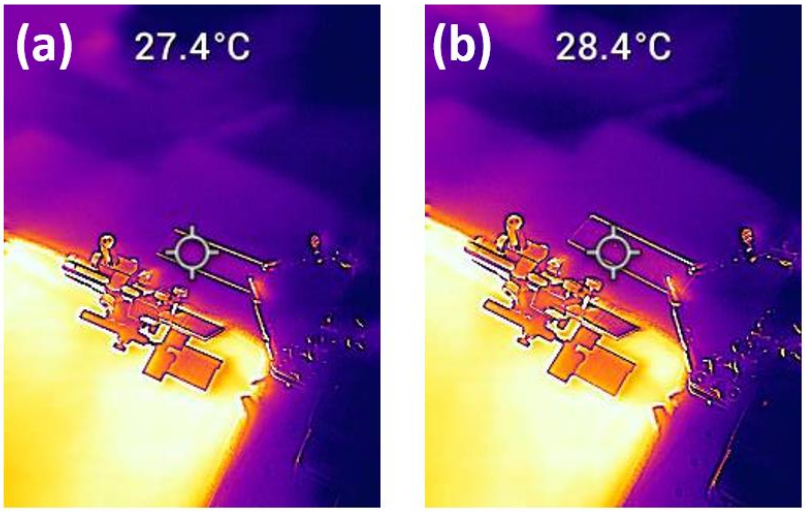

Fig. B.5: Thermal camera images for (a) bare glass slide (b) MIM sample #3 measured under thermal camera crosshair.

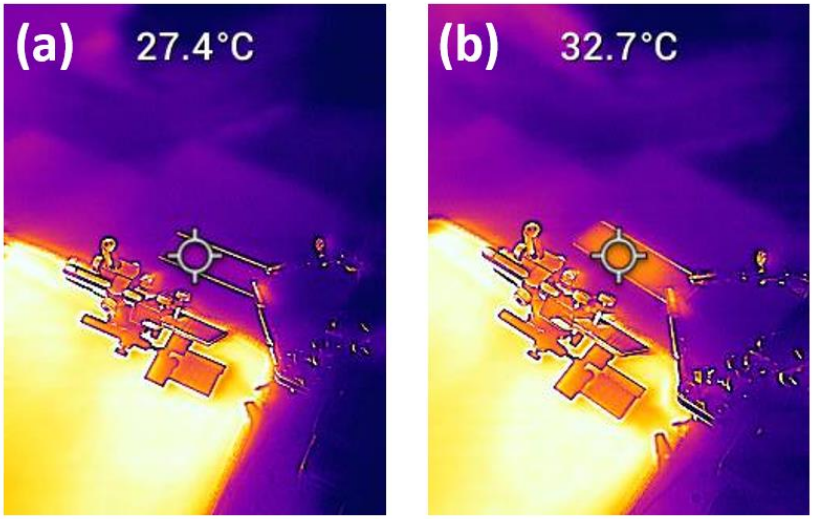

Fig. B.6: Thermal camera images for (a) bare glass slide (b) MIM sample #4 measured under thermal camera crosshair.

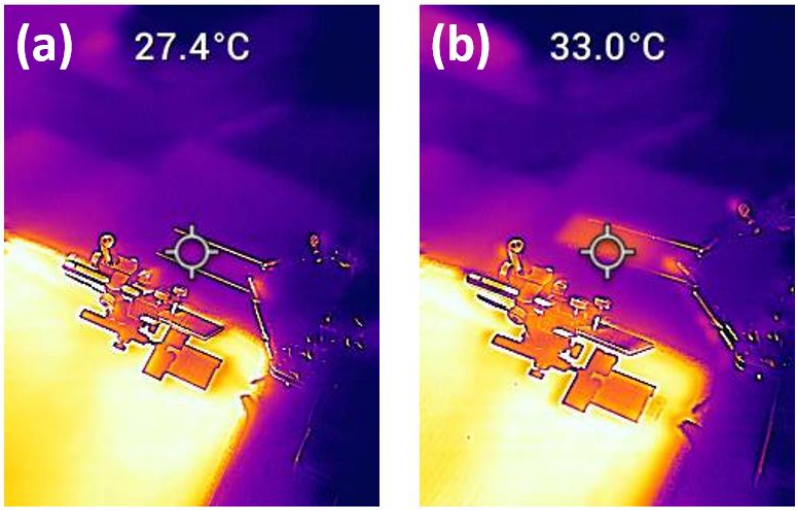

Fig. B.7: Thermal camera images for (a) bare glass slide (b) MIM sample #5 measured under thermal camera crosshair.

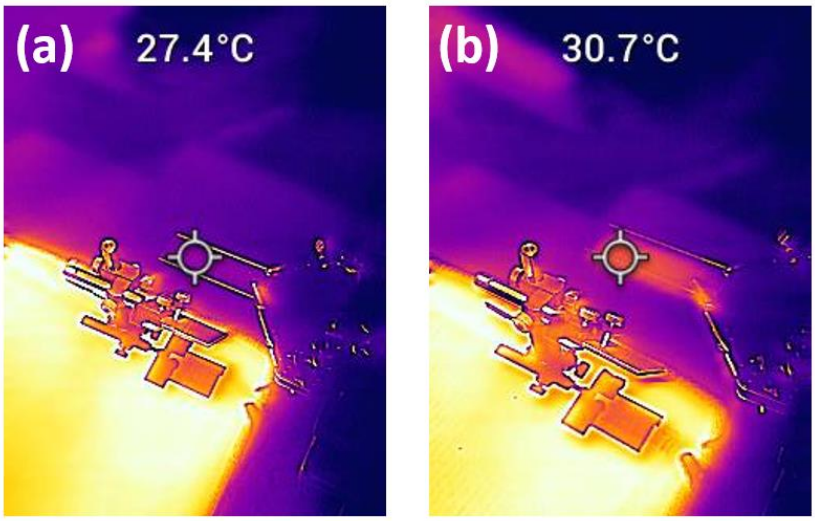

Fig. B.8: Thermal camera images for (a) bare glass slide (b) MIM sample #6 measured under thermal camera crosshair.

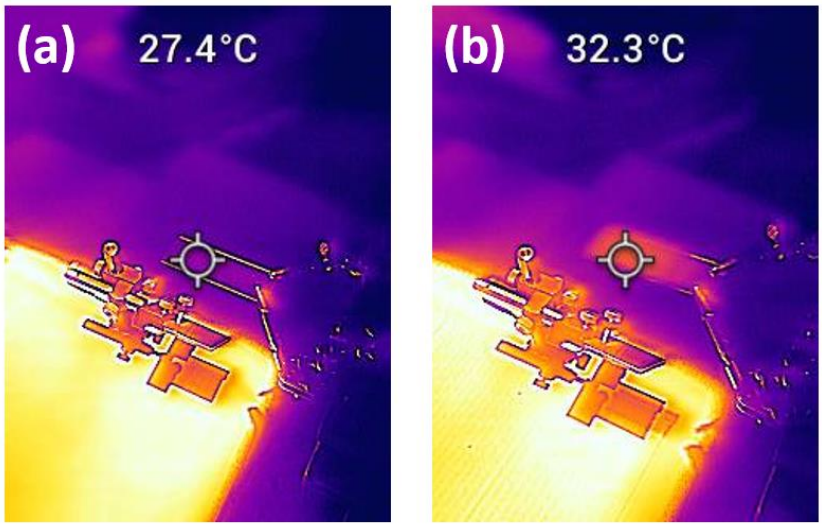

Fig. B.9: Thermal camera images for (a) bare glass slide (b) MIM sample #8 measured under thermal camera crosshair.

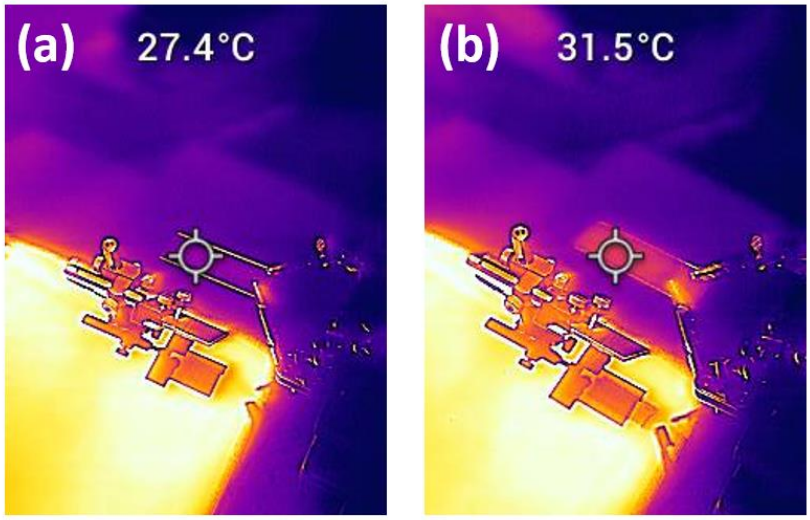

Fig. B.10: Thermal camera images for (a) bare glass slide (b) MIM sample #9 measured under thermal camera crosshair.

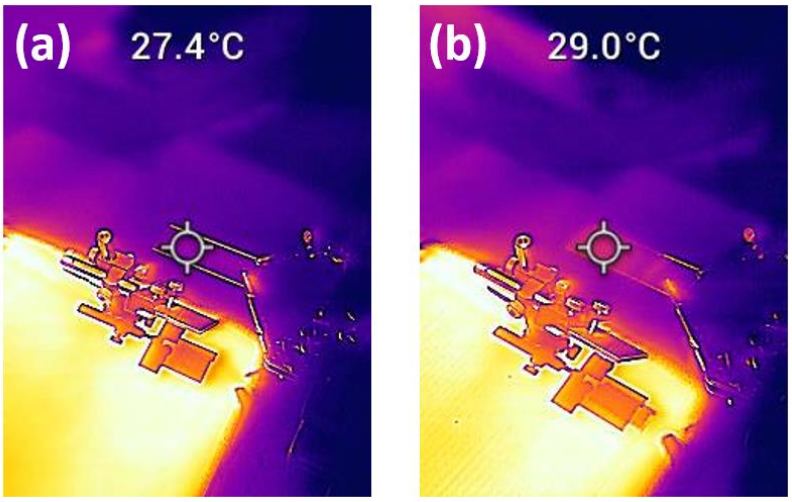

Fig. B.11: Thermal camera images for (a) bare glass slide (b) MIM sample #10 measured under thermal camera crosshair.